2016

Comparisons of seismic interferometry by cross correlation, deconvolution, and cross coherence

Haitao Cao
Michigan Technological University, haitaoc@mtu.edu

COMPARISONS OF SEISMIC INTERFEROMETRY BY CROSS CORRELATION, DECONVOLUTION, AND CROSS COHERENCE

By

Haitao Cao

A THESIS

Submitted in partial fulfillment of the requirements for the degree of

MASTER OF SCIENCE

In Geophysics

MICHIGAN TECHNOLOGICAL UNIVERSITY

2016

This thesis has been approved in partial fulfillment of the requirements for the Degree of MASTER OF SCIENCE in Geophysics.

Department of Geological and Mining Engineering and Sciences

Thesis Co-Advisor: *Dr. Wayne D. Pennington*

Thesis Co-Advisor: *Dr. Roohollah Askari*

Committee Member: *Dr. Gregory P. Waite*

Department Chair: *Dr. John S. Gierke*

Table of Contents

List of Figures

Acknowledgement

Foremost, I would like to express my sincere gratitude to my advisors Dr. Wayne D. Pennington and Dr. Roohollah Askari for their continuous expert guidance, warm encouragement and constructive criticism throughout my research. Without their guidance and persistent help, this thesis would have remained a dream. In addition, I am thankful for Dr. Gregory Waite having served on my committee.

My appreciation also extends to graduate fellows in SPOT lab with whom we shared ideas and encouraged each other. I am very thankful to Simisola Arogundade for providing me the background information of my research. Her support and assistance made my thesis go smoothly.

I also appreciate Dr. Jan Thorbecke at Delft University of Technology, Netherland. Without his Finite difference modeling codes, it would be hard for me to progress my research. In addition, I want to thank Prof. Christopher Juhlin at Uppsala University, Sweden and Dr. Stefan Lüth from GFZ German Research Center for sharing the field data acquired at Ketzin and their advice for data processing. In addition, I wishes to thank Seismic Unix from the Colorado School of Mines, Center for Wave Phenomena.

Finally but most important, I would like to express my deepest thanks to my beloved parents and brother for their encouragement and supports.

Abstract:

Ambient noise seismic interferometry (ANSI) has been applied widely for geophysical investigations including earthquake tomography, civil engineering and seismic exploration purposes. Comparing this approach with the traditional active seismic survey, the application of ANSI is cost effective, environmentally friendly and easily repeatable. Conventional seismic interferometry by cross correlating wavefields recorded at different receivers has already obtained fruitful results.

Even though the application of seismic interferometry (SI) by cross correlation has been successful, different methods for the processing workflow such as cross coherence and deconvolution have been conducted in an effort to improve the resolution. While these three methods have been evaluated for shear wave imaging of the near surface using surface waves by other authors, no conclusive study has been performed to compare the results from these methods for reflection surveys. In this study, by considering three common methods of retrieving a virtual seismic record, I compare the methods and analyze the results with respect to their signal-to-noise ratios.

I applied ANSI to numerically modeled data to retrieve reflection responses for both base and repeat surveys monitoring the time-lapse changes of the impedance at the top of a reservoir before and after CO_2 injection. The retrieved seismic response by the three methods including cross correlation, deconvolution and cross coherence are also compared for the field noise data recorded near the CO_2 storage site in Ketzin, Germany. While all three provide adequate results in noise-free synthetic data examples, the cross coherence method yielded improved images using real data.

1. Introduction

Conventional seismic interferometry (SI) constructs Green's function between two receivers where a seismic response is obtained from cross correlating wavefields excited by a noise source recorded by those two receivers. This seismic response is regarded as a virtual signal recorded at one receiver from a virtual source originating at the position of the other receiver. Seismic interferometry was initially introduced by Claerbout (1968) for an acoustic layered medium: one side of the autocorrelation of the transmission response at depth is equal to the reflection response. His idea of applying the result to a 3D scenario has been addressed by use of the stationary phase method (Schuster, 2001; Snieder 2004; Schuster and Zhou, 2006). Weaver and Lobkis (2001, 2002) investigated the 3D scenario for diffuse elastic waves (the waves spread out with same strength). Using one-way reciprocity theorems without the assumption of diffusivity of the wavefield (Wapenaar et al., 2004; Wapenaar and Fokkema, 2006), the relations between reflection and responses for 3D inhomogeneous media were constructed by passive noise sources in the subsurface, also known as acoustic daylight imaging. Schuster et al., (2004) extended daylight imaging to arbitrary source numbers or distributions.

For different purposes, seismic interferometry is used to retrieve surface wave and body wave responses respectively. Researchers have been extracting the earth structure information by retrieving the surface wave from seismic interferometry (Shapiro and Campillo 2004, 2005; Sabra et al., 2005b; Ritzwoller et al., 2005; Gerstoft et al., 2006; Larose et al., 2004, 2006a, 2006b; Yao et al., 2006; Gumundsson et al., 2007; Nunziata et al., 2009). Surface wave retrieval has generated robust results due to the strong

recorded signals compared with those of body waves. Unfortunately, the resolution of surface wave seismic interferometry has been relatively insufficient to extract information from deep layers for exploration purposes because the distribution of ambient noise source is more limited in frequency content (and largely outside of the range of interest), and amplitude decay is larger than for surface waves (Draganov et al., 2009 and 2013; Xu et al., 2012). Nevertheless, some studies have been conducted to extract body waves from teleseimic arrivals and ambient noise (Roux et al., 2005; Kumar and Bostock, 2006; Tonegawa et al., 2009; Zhang et al., 2009; Nakata et al., 2011; Xu et al., 2012). In addition to passive seismic interferometry, active seismic interferometry, which uses active sources instead of ambient noise, has been developed (Panea et al., 2014). However, passive seismic interferometry remains more common than its active counterpart due to its cost efficiency and fewer logistic and environmental concerns. The ambient noise used in ambient passive seismic interferometry (ANSI), is initiated from different sources (not necessarily seismic ones) such as transportation, architectural construction, teleseismic events, and the dynamic changes of deep reservoirs due to production and rock compaction.

Providing good resolution, passive seismic interferometry can be used as an alternative to active source seismic surveys used in such applications as seismic exploration, time-lapse monitoring, and civil engineering. For instance, from ten hours of passive seismic noise data acquired in a desert area, Draganov (2007) obtained coherent reflection events that were comparable with the results of an active seismic survey. Cheraghi et al., (2015) imaged the ore deposits in a crystalline rock environment from 300 hours of ambient noise generated by underground mining activities. Applying the method to earthquake-

recorded data, Nakata and Snieder (2012) analyzed shear wave velocity changes in a small region using "noise" from three significant earthquakes.

ANSI can significantly reduce the operational cost and environmental concerns of time-lapse monitoring. Time-lapse monitoring is the process of measuring multiple vintages of seismic surveys where the acquisition is repeated at the same location. This procedure has been widely used for CO_2 sequestration and enhanced oil recovery (Lumley, 2001). For instance, Xu et al. (2012) reconstructed the subsurface structure at the Ketzin experimental CO_2 storage site in Germany by cross correlating the approximately 25 hours' recorded ambient noise. Boullenger et al. (2015) applied numerical feasibility study and field data test for ANSI at Ketzin CO_2 storage site.

In order to obtain optimal resolution from passive seismic interferometry, we must optimize all acquisition and processing parameters. Several studies have been conducted to characterize the best possible acquisition and processing configurations for passive seismic interferometry. For instance, Mehta and Snieder (2008) applied synthetic models to show acquisition geometry requirements, including allowable source spacing and source-receiver distributions, for generating virtual-source data. Bensen et al., (2007) summarized the processing procedures for seismic ambient noise data to obtain reliable broad-band surface waves. Mehta et al., (2007) demonstrated that wavefield separation can overcome the limitations of acquisition aperture that results in artifacts, improving the quality of retrieved virtual source data.

In this study, by considering three common methods of retrieving a virtual seismic record, cross-correlation, cross-coherence, and deconvolution, I compare the results visually and

using measures of signal-to-noise. Cross-correlation refers to cross correlating the recording of noise received at different receivers. Cross coherence, as used in seismology and engineering (Aki, 1957; Bendat and Piersol, 2000; Prieto et al., 2009), is a normalization algorithm applied to the spectral amplitudes of recorded signals, in the frequency domain. Deconvolution cancels the power spectrum of source signal (Mehta et al., 2007; Vasconcelos and Snieder, 2008); Nakata et al., (2013) applied deconvolution interferometry to monitor a building for damage analysis using recorded earthquake tremors. Although these three methods have been evaluated for real shear wave imaging of near surface using surface waves (Nakata et al., 2011), no conclusive study has been performed to compare their results for reflection surveys.

In my thesis, I used a 2D finite difference program (Thorbecke, 2011) to model ambient noise originating from deep structures for a given velocity model. I applied cross correlation, deconvolution and cross coherence algorithms to the data to generate the virtual seismic records. I assessed the quality of the obtained seismic images from these methods. In addition, by applying a slight change to the acoustic impedance of a formation in my model, I simulated a scenario resembling CO_2 sequestration. By subtracting the seismic images of the base line from that of monitoring, I showed the potential of the method for CO_2 sequestration monitoring. The retrieved seismic response by the three methods including cross correlation, deconvolution and cross coherence are also compared for the field noise data recorded near the CO_2 storage site in Ketzin.

2. Theory

2.1 Interferometry by cross correlation

We first introduce the Green's function that is applied to the seismic interferometry. A wavefield generated by a source is represented by the convolution of a source wavelet and a Green's function (Wapenaar et al., 2010). For instance, if we assume a wavefield $u(r,s)$ generated by a source at "s" and a receiver at "r", without considering the additive noise, the wavefield $u(r,s)$ can be described as the product of the source wavelet and the Green's function in frequency domain

$$u(r,s) = w(s)\, G(r,s), \tag{1}$$

where $w(s)$ is the source wavelet and (r,s) is the Green's function. If we have two receivers x_A and x_B and a source x_s along a line, the response recorded at the receivers in time domain can be denoted as

$$u(x_A, x_s, t) = G(x_A, x_S, t) * w(t), \tag{2}$$

$$u(x_B, x_s, t) = G(x_B, x_S, t) * w(t). \tag{3}$$

The cross correlation of the Green's function representation in 1D is

$$G(x_B, x_A, t) = G(x_B, x_s, t) * G(x_A, x_S, -t)\ , \tag{4}$$

$$G(x_B, x_A, -t) = G(x_B, x_S^{(i)}, t) * G(x_A, x_S^{(i)}, -t). \tag{5}$$

By combining Equations 4 and 5, and replacing the impulsive point source by field noise source with wavelet $w(t)$, we obtain

$$\{G(x_B, x_A, t) + G(x_B, x_A, -t)\} * W_s(t) = \sum_{i=1}^{2} u\left(x_A, x_S^{(i)}, t\right) *\ u\left(x_B, x_S^{(i)}, t\right), \tag{6}$$

where $W_s(t)$ represents the autocorrelation of the wavelet, and the asterisk demotes the temporal convolution.

Because random noises are uncorrelated with their own spectra, the observed wavefield excited by two noise source $\widehat{N}(x,\omega)$ and $\widehat{N}(x',\omega)$ at positions x and x' are

$$\widehat{u}(x_A,\omega) = \oint_S \widehat{G}^*(x_A,x,\omega)\,\widehat{N}(x,\omega)d^2x, \tag{7}$$

$$\widehat{u}(x_B,\omega) = \oint_S \widehat{G}^*(x_B,x,\omega)\,\widehat{N}(x',\omega)d^2x, \tag{8}$$

while the noise sources satisfy the relation

$$\langle \widehat{N}^*(x',\omega)\widehat{N}(x,\omega)\rangle = \delta(x-x')\hat{S}(\omega), \tag{9}$$

where $\langle\ \rangle$ represents the spatial ensemble average; $\hat{S}(\omega)$ is the average power spectrum of the uncorrelated noise. Thus, in the frequency domain for the mutually uncorrelated noise source, Equation (6) can be written as (Wapenaar, 2006)

$$\begin{aligned}\left\{\hat{G}(x_B,x_A,\omega) + \hat{G}^*(x_B,x_A,\omega)\right\}\hat{S}(\omega) &\approx \frac{2}{\rho c}\langle \hat{u}^*(x_A,\omega)\hat{u}(x_B,\omega)\rangle \\ &= \oint_S \hat{G}^*(x_A,x,\omega)\,\hat{G}(x_B,x,\omega)\hat{S}(\omega)d^2x,\end{aligned} \tag{10}$$

where ρ and c represent density and velocity respectively. The cross correlation of the wavefields recorded at receiver r_A and r_B is given by (Wapenaar et al., 2011)

$$C_{AB} = \hat{u}^*(r_A,\omega)\,\hat{u}(r_B,\omega) = |S(w)|^2 G(r_A,x)G(r_B,x). \tag{11}$$

In passive reflected-wave interferometry, errors of the retrieved seismic response might be encountered when the algorithm is applied to the field noise data, resulting from the assumption that the waves propagate perpendicular to the closed source boundary. In this situation, the closed boundary is replaced by an open free surface which might contribute to the one-sided illumination generating spurious multiples. Even though the amplitude is not reliable, the phase information is still accurate.

2.2 Interferometry by deconvolution

Snieder et al., (2006) introduced the interferometry based on the deconvolution approach and applied it to monitoring velocity changes of a building response using earthquake signals (Nakata et al., 2013). Snieder et al., (2006, 2009) and Vasconcelos and Snieder (2008) described the application to a general geometry of a source and receivers. I follow their derivation here. Given a wavefield as $u(r_{A,B}, s) = G(r_{A,B}, s)W(s)$ in frequency domain, the deconvolution is obtained by

$$D(AB) = \frac{u(r_A,s)}{u(r_B,s)} = \frac{G(r_A,s)}{G(r_B,s)} = \frac{G(r_A,s)G^*(r_B,s)}{|G(r_B,s)|^2}. \quad (12)$$

As in cross-correlation, the source signature is canceled in the deconvolution approach. The numerator $G(r_A, s)G^*(r_B, s)$ in Equation (12), which is similar to the term in cross correlation (Equation 11), suggests that the two methods might have similar outputs, especially when the denominator $|G(r_B, s)|^2$ is a smooth function. But in practice, the power spectrum of the Green's function varies significantly with frequency when there is an overlap of interfering waves. Particularly, in the case that the wavefield recorded at r_A is coincident with that of r_B, Equation (12) becomes $D(AB) = 1$ corresponding to $D_{AB}(t) = \delta(t)$ in time domain. This can be interpreted that the deconvolved result equals zero except at non-zero time because of the $\delta(t)$ function. Mathematically, it is a clamped boundary condition (Vasconcelos and Snieder, 2009).

2.3 Interferometry by cross coherence

Coherence, along with the semblance, which is related to a normalized cross-correlation, was first introduced by Neidell (1971) to determine stacking velocities for multichannel seismic data. In 2009, Prieto et al., presented the relationship between spatial coherency of ambient noise field and Green's function in both time and frequency domains. Prieto et al (2009) also expounded that the information of earth structure can be extracted by applying spatial coherency of the ambient seismic field (Prieto et al., 2009). Nakata and Snieder (2011) demonstrated the spatial coherency by cross coherence and constructed Green's function between two points as

$$H_{AB} = \frac{u(r_A,s)u^*(r_B,s)}{|u(r_A,s)||u(r_B,s)|}. \quad (13)$$

The equation can be written by replacing the wavefield with the product of Green's function and wavelet $W(s)$ in the frequency domain as

$$H_{AB} = \frac{G(r_A,s)G^*(r_B,s)}{|G(r_A,s)||G(r_B,s)|}. \quad (14)$$

where $u(r_{A,B}, s)$ denotes the wavefield recorded at receivers *A* and *B*, and the asterisk represents the complex conjugate. From Equation (13), we can easily find that the numerator is the same as the expression in cross correlation (11) before adding the source wavelet, but divided by the product of their own absolute values. Thus, the phase information of each wavefield remains, and the amplitude information is removed. Since the original amplitude information is normalized in cross-coherence, the amplitude related studies such as amplitude-versus-offset, or bright-spot or dim-spot analysis, cannot be investigated. From the above expression, the wavelet is also canceled, similar

to the deconvolution method. Receivers sometimes record high amplitude noises initiated by poor geophone coupling, instrumentation problems, or near surface sources; cross coherence can overcome these dramatic amplitude variations.

3. Methodology

3.1 Passive noise modeling

The programming code that I used to model the synthetic noise is an open-source finite-difference code developed by Thorbecke and Draganov (2001). A velocity model of an acoustic media was created with noise sources placed in the deeper layers (Figure 3.1), following a method substantiated by Thorbecke and Draganov (2001) and by Boullenger et al. (2015). In contrast, for an elastic media, *P* and *S* wave velocities and *Q* factor have to be considered including Q_p and Q_s for all geological layers. The more complex parameters in an elastic media model is high potentially generate undesirable result if the parameters are not carefully chosen. Therefore, in this thesis only acoustic medium is applied. The black dots in the deep formation in Figure 3.1 mark the locations of the 1000 noise sources.

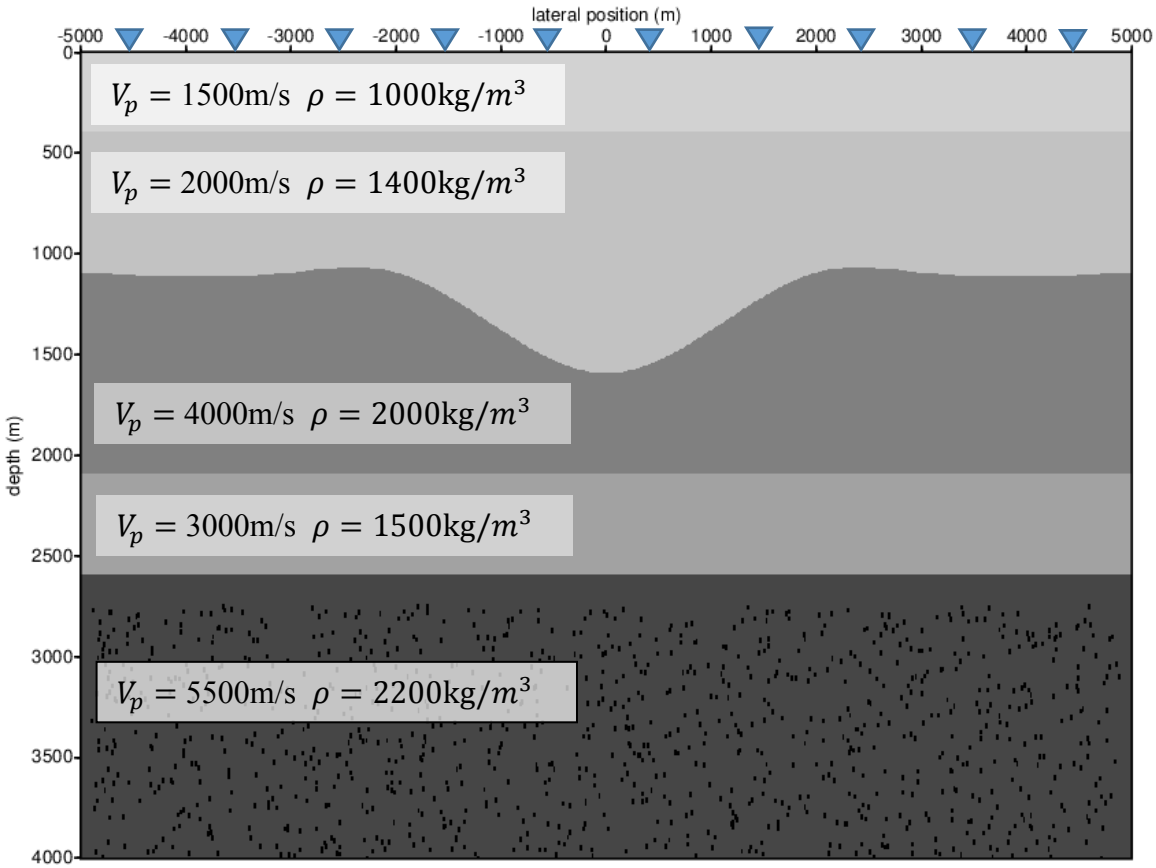

Figure 3.1. An acoustic model with 1000 noise sources randomly distributed in the deep layer with the depth between 2700m and 4000m. The black dot marks the noise source and 201 receivers are placed on the free surface at every 50m represented by ▼.

The finite difference approximation has a limitation that could cause strong dispersion for the 2D wave equation, if the following relation is not satisfied (Thorbecke and Draganov, 2001).

$$\Delta h < C_{min}/5f_{max}. \qquad (15)$$

where Δh is the discretization step which is equal to the grid size in finite difference scheme, C_{min} denotes the minimum P wave velocity, and f_{max} represents the maximum frequency of the signals from the noise sources.

Figure 3.2a shows 20 random noise signals with the sampling rate of 0.008s and different time duration (the maximum time duration is 10s). To suppress dispersion, the maximum frequency of the source wavelet is assumed to be 30Hz. Figure 3.2b and Figure 3.2c show the signature and amplitude spectra of one random source noise. These individual sources activate at random times and their signals typically overlap, creating a very long sequence of random composite signal. Both the base and repeat survey in the following discussion obey the same noise source signature and distribution.

(a) 20 random noise

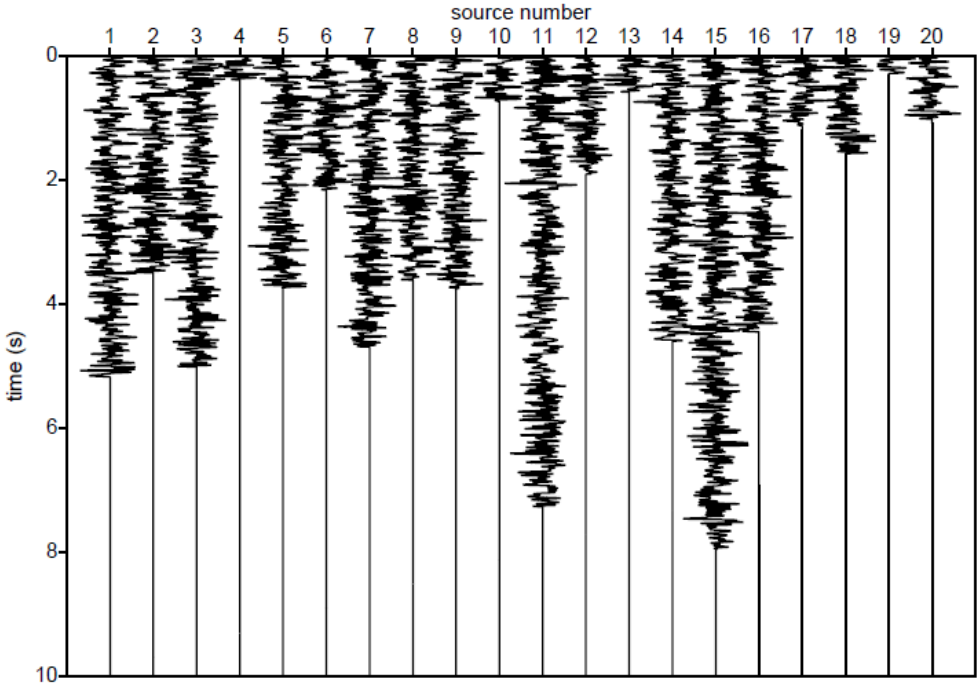

(b) One source signature.

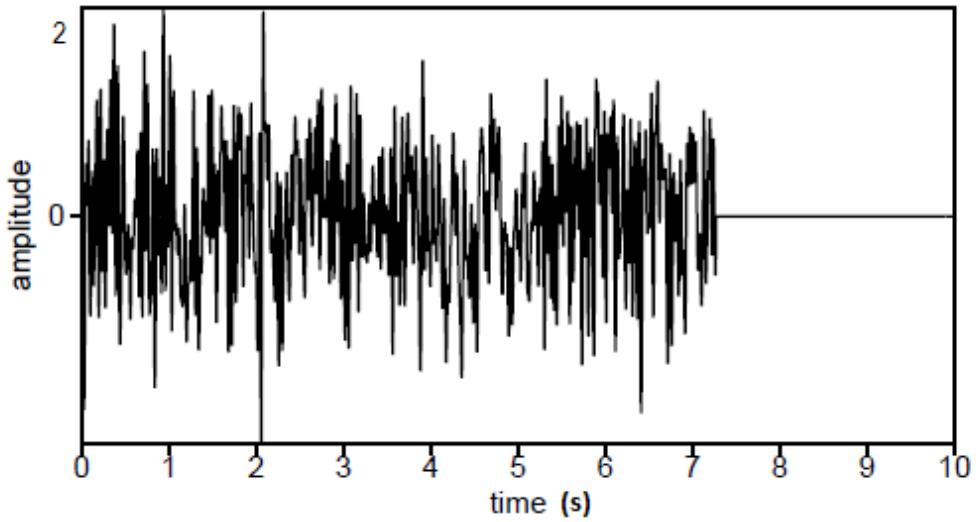

(c) One source amplitude spectrum with max frequency at 30 HZ.

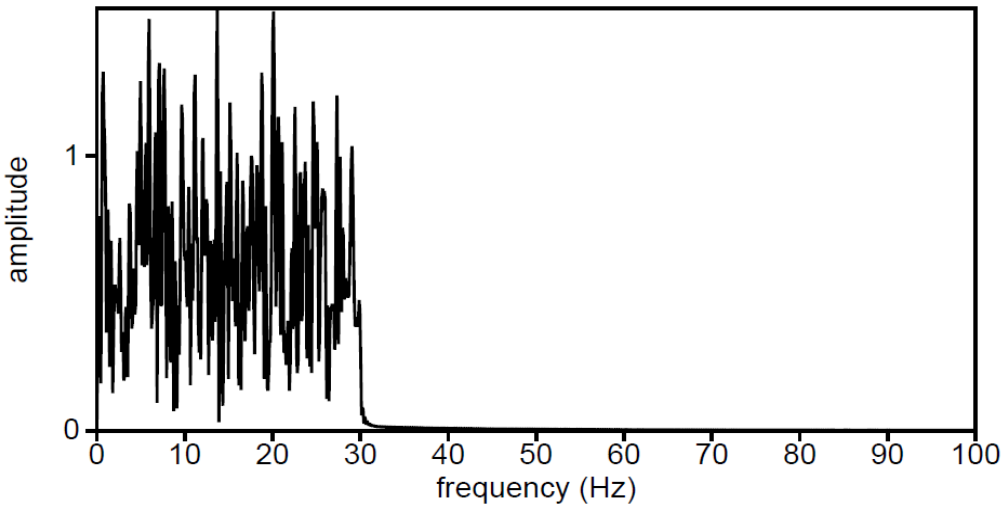

Figure 3.2. (a) The 20 random noise signatures with varying source duration: (b) One source signature: (c) The amplitude spectrum of the source signature in 1(b).

3.2 The syncline case

The geological model shown in Figure 3.1 is 10,000 m wide and 4000 m deep with 201 receivers regularly spaced on the flat surface. Signals from the 1000 noise sources are recorded at all receivers. Figure 3.3 provides examples from 65-s time windows (out of a total recording time window of 120 s) from 21 of the receivers within a 1000-m wide lateral segment.

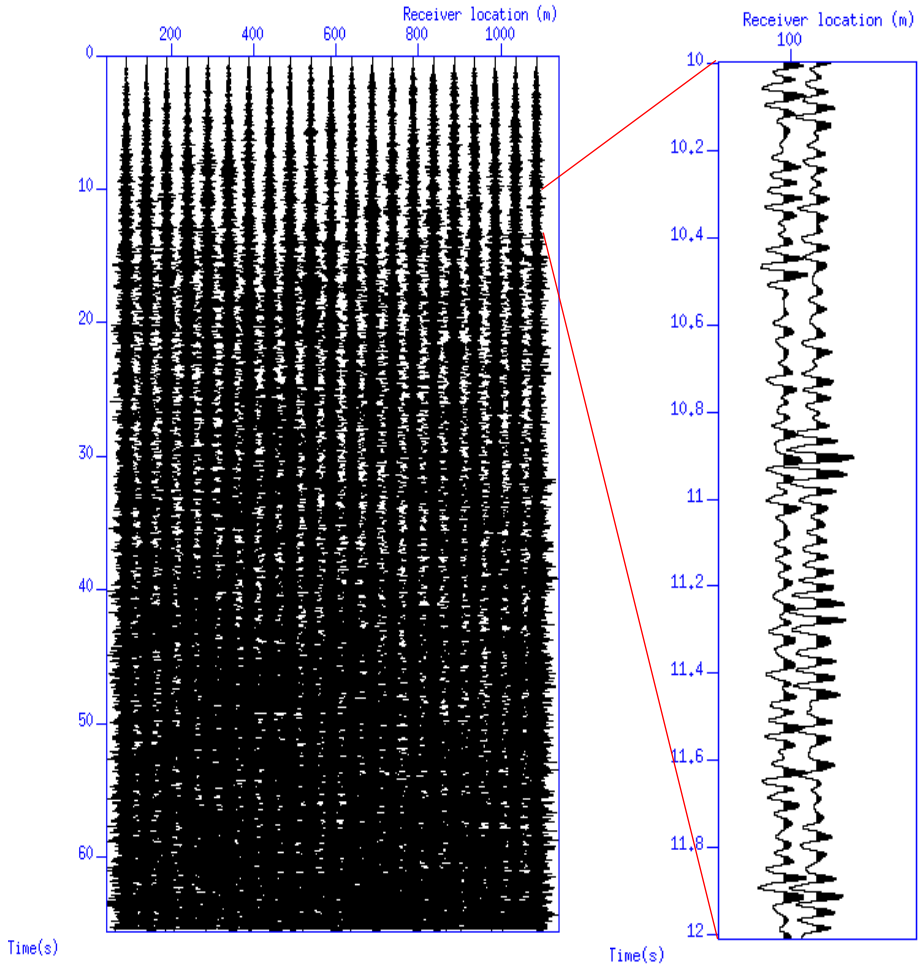

Figure 3.3. On the left, 21 recorded traces are demonstrated among the entire 201 traces. On the right side, it is a 2s window from the left side

To generate the virtual shots by seismic interferometry, we apply cross-correlation, deconvolution, or cross coherence to a reference trace with the other traces. Figures 3.4a-3.4c compare a virtual shot record (common-shot gather) resulting the cross-correlation (a), cross coherence (b), and deconvolution (c) of the middle trace with other traces.

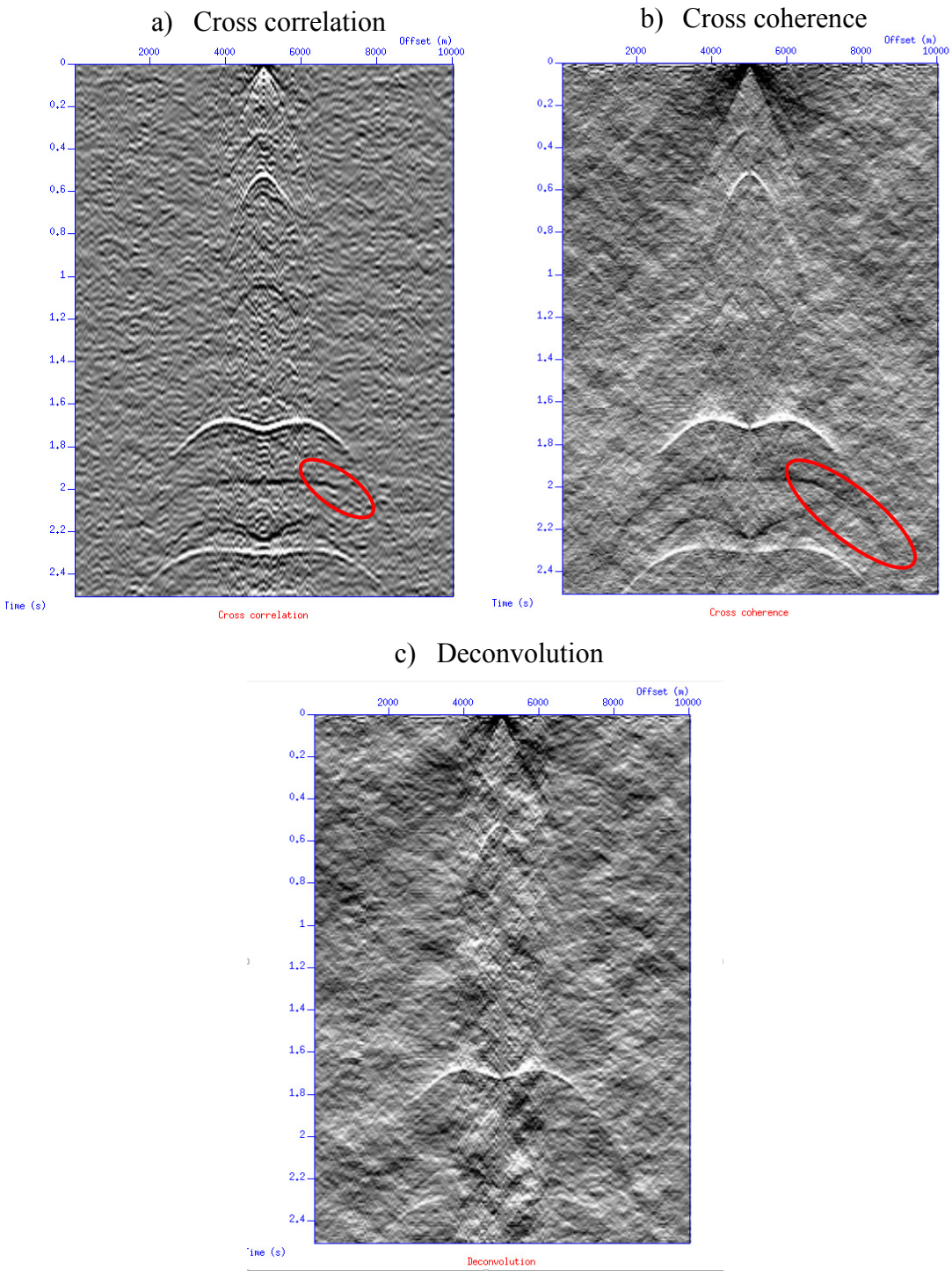

Figure 3.4. Virtual common shot gather retrieved at location of receiver 101 for cross correlation, cross coherence and deconvolution methods from the syncline geological model. The reflector starting in 1.98s is compared in marked by red elliptic.

In the cross correlation virtual shot (Figure 3.4a), all four primary reflections, at two-way travel times of 0.53s, 1.73s, 1.98s and 2.31s, are successfully retrieved and recognized from their hyperbolic moveouts at far offsets; the direct wave is also retrieved and recognized by its linear moveout. Visually, the cross coherence method seems to provide the most distinct resolution of the primary reflectors, with an apparent high signal-to-noise ratio. The deconvolution method seems to provide the weakest illumination of the reflectors with the apparently lowest signal-to-noise ratio.

Of the three methods, we observe that the virtual common shot gather generated by cross-coherence method is clearer and more coherent than those from the cross correlation and deconvolution methods. The reason is cross coherence only keeps phase information, the various amplitude effects are removed.

In the next step, I merged the virtual shots and sorted them into CMP gathers. After applying NMO (determined by velocity analysis, and confirmed by comparison with root-mean-square velocity from the model velocities) to the CMP gathers, the reflected events are mostly flattened (Figure 9.1). The two way travel time in stacked section from the three methods (Figure 3.5) corresponds to the geological model built by the 2D finite difference method.

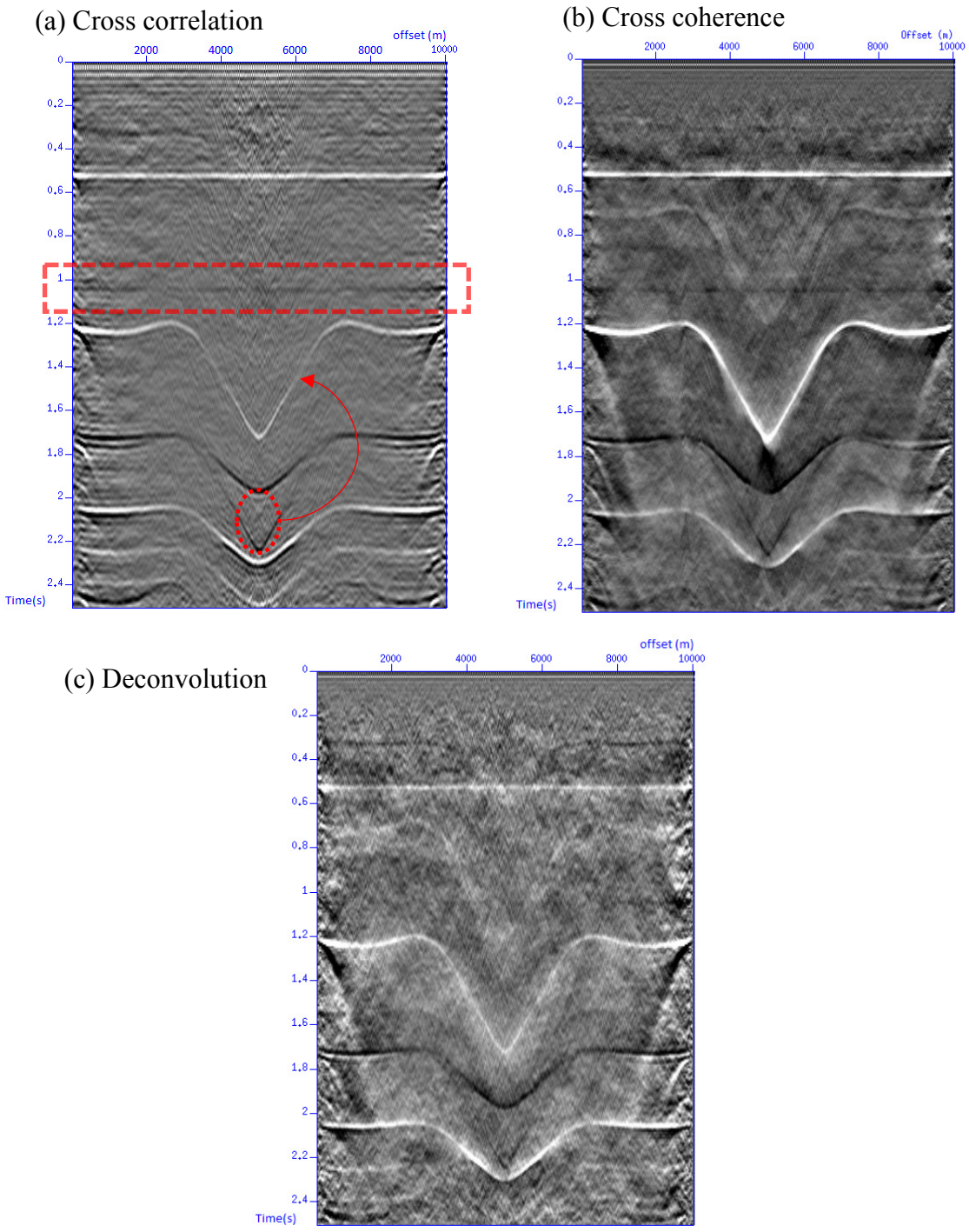

Figure 3.5. The post stack unmigrated image of the first 2.5s data by cross correlation, cross coherence and deconvolution methods. Multiples are marked in the cross correlation.

We mark a flat-lying multiple reflection in the red dashed rectangular at near 1.06 s in the cross-correlation section (Figure 3.5a) but note that it is also present in the cross-coherence and deconvolution cases. Moreover, we notice that a peg-leg multiple emerges below the third reflected event around 1.75 s marked by the red circle in Figure 3.5a. The peg-leg multiple path includes a reflection between the free surface and the shallowest reflector (at 0.53s) as well as the reflection from the deeper (~1.2s) interface. We also note an unusual artifact layer around 0.7 s in the cross-coherence and deconvolution cases, mirroring the ~1.2s reflector, but above it. We will investigate the effect of "regularization" to remove the artifact layer in the next case, that of an anticline.

3.3 The anticline case study and CO_2 injection simulation

A reservoir is modeled at a depth around 2000 m intended to be a repository for CO_2 injection. Figure 3.6 and Figure 3.7 show the geological models for before and after CO_2 injection respectively that are used to simulate seismic time lapse. The noise signature and distribution are the same as the syncline case for both base and repeat passive surveys. The images of the retrieved base and repeat stacked section and the difference between the base and repeat surveys by cross correlation, cross coherence and deconvolution method are shown in Figure 3.8, Figure 3.9 and Figure 3.10 respectively.

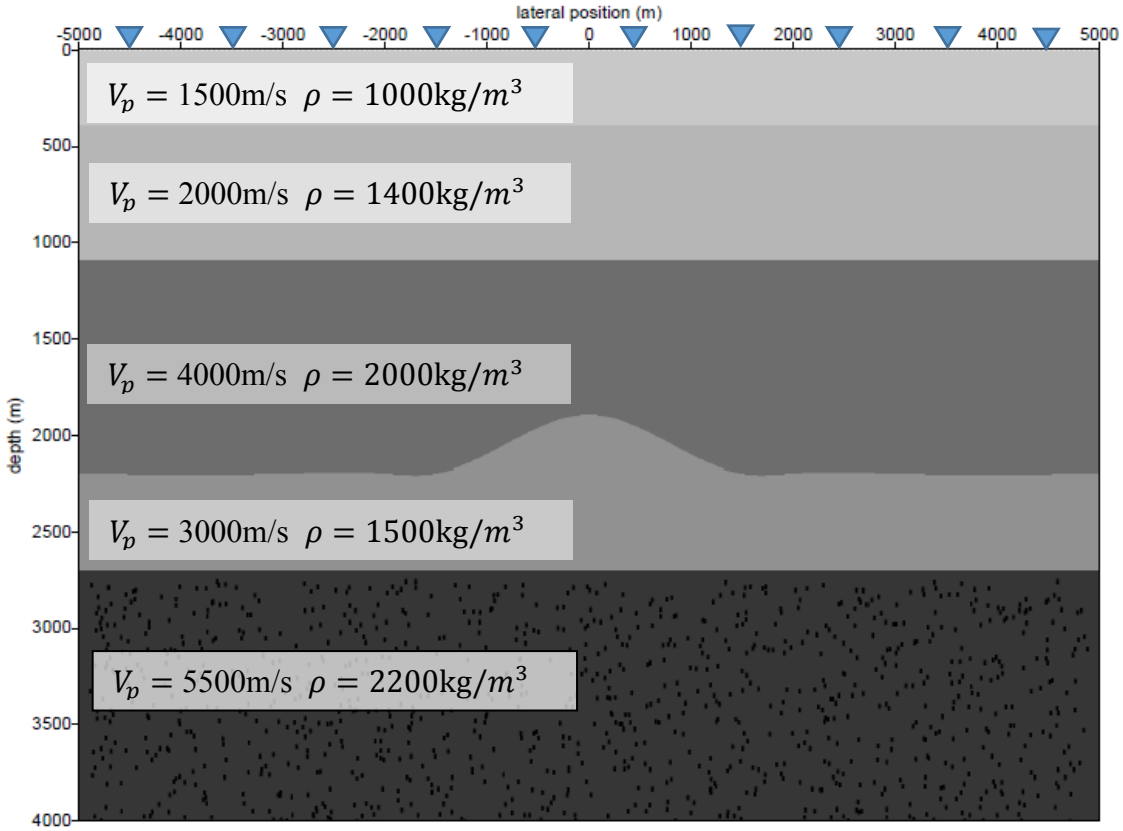

Figure 3.6. An acoustic model of anticline which represents the location of a reservoir. The noise sources distribution, receivers geometry and elastic property is the same as syncline model shown in Figure 3.1.

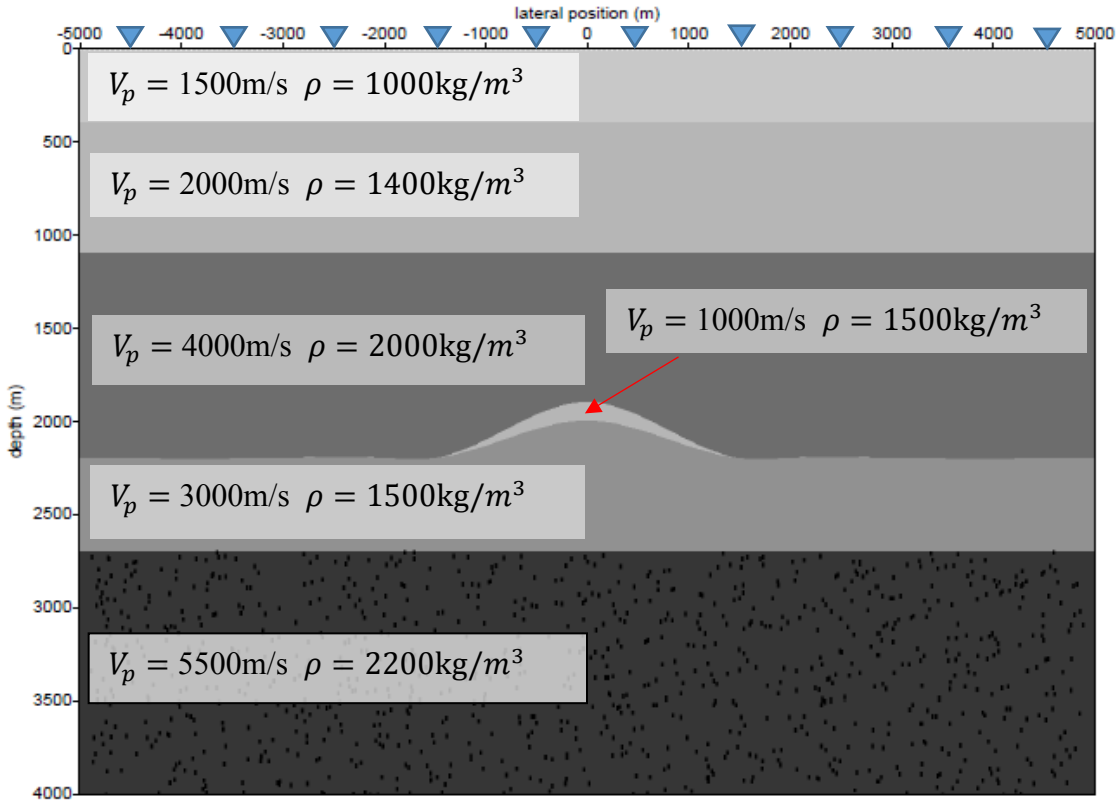

Figure 3.7. The geological model of a dynamic change of the reservoir after CO_2 injection. The velocity of P wave and mass density decreased on the top of the reservoir due to CO_2 injection. The noise sources distribution, receivers geometry and elastic property is the same as syncline model shown in Figure 3.1.

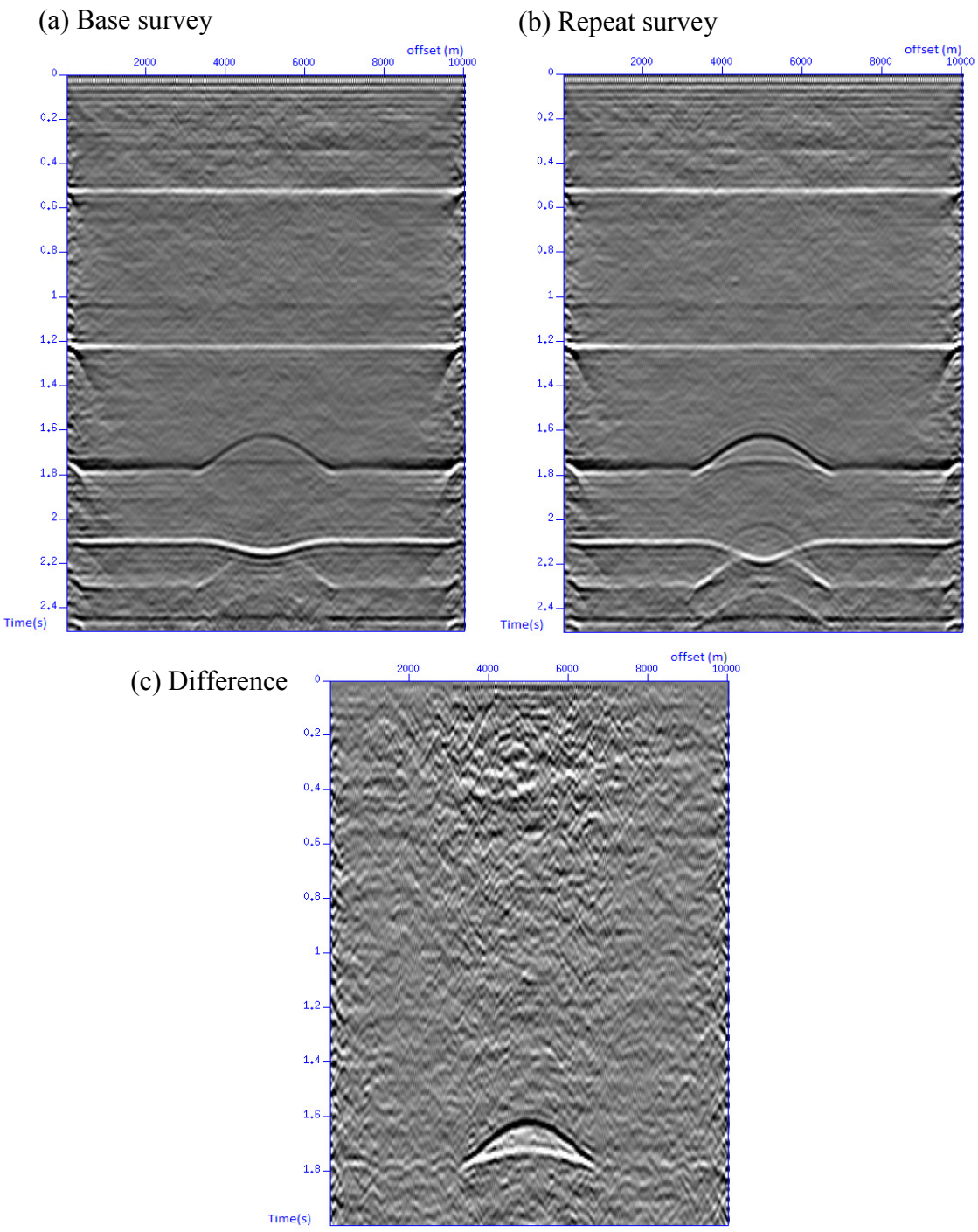

Figure 3.8. Stacked images from cross correlation method for the time lapse reservoir monitoring simulation. (a) The stacked section for the base survey before CO_2 injection. (b) Stacked section for the repeat survey after CO_2 injection. (c) The difference between the repeat and base survey.

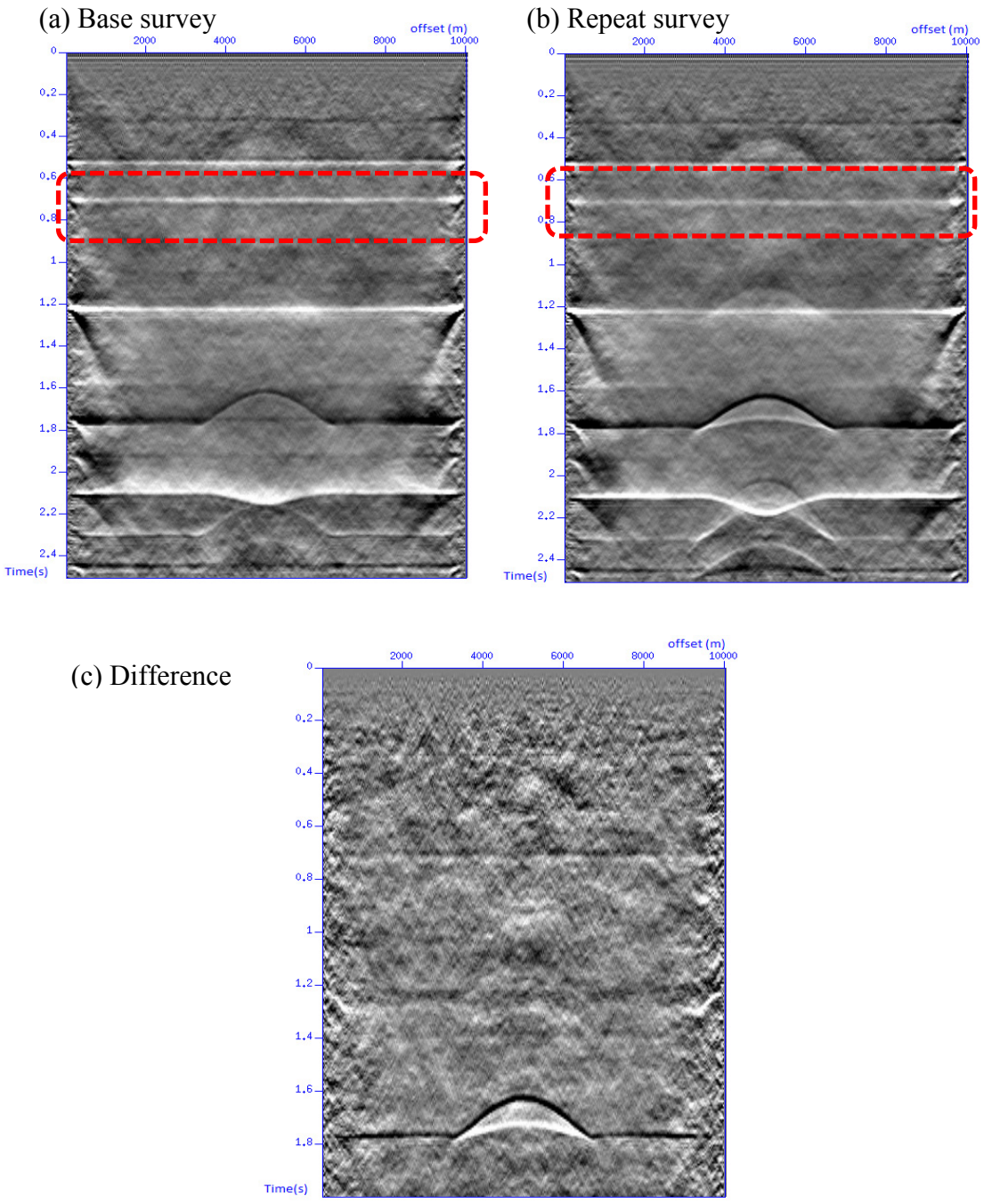

Figure 3.9. Stacked images from cross coherence method for the time lapse reservoir monitoring simulation. (a) The stacked section for the base survey before CO_2 injection. (b) Stacked section for the repeat survey after CO_2 injection. (c) The difference between the repeat and base survey. The artificial reflection around 0.7s is indicated inside the red dashed rectangular.

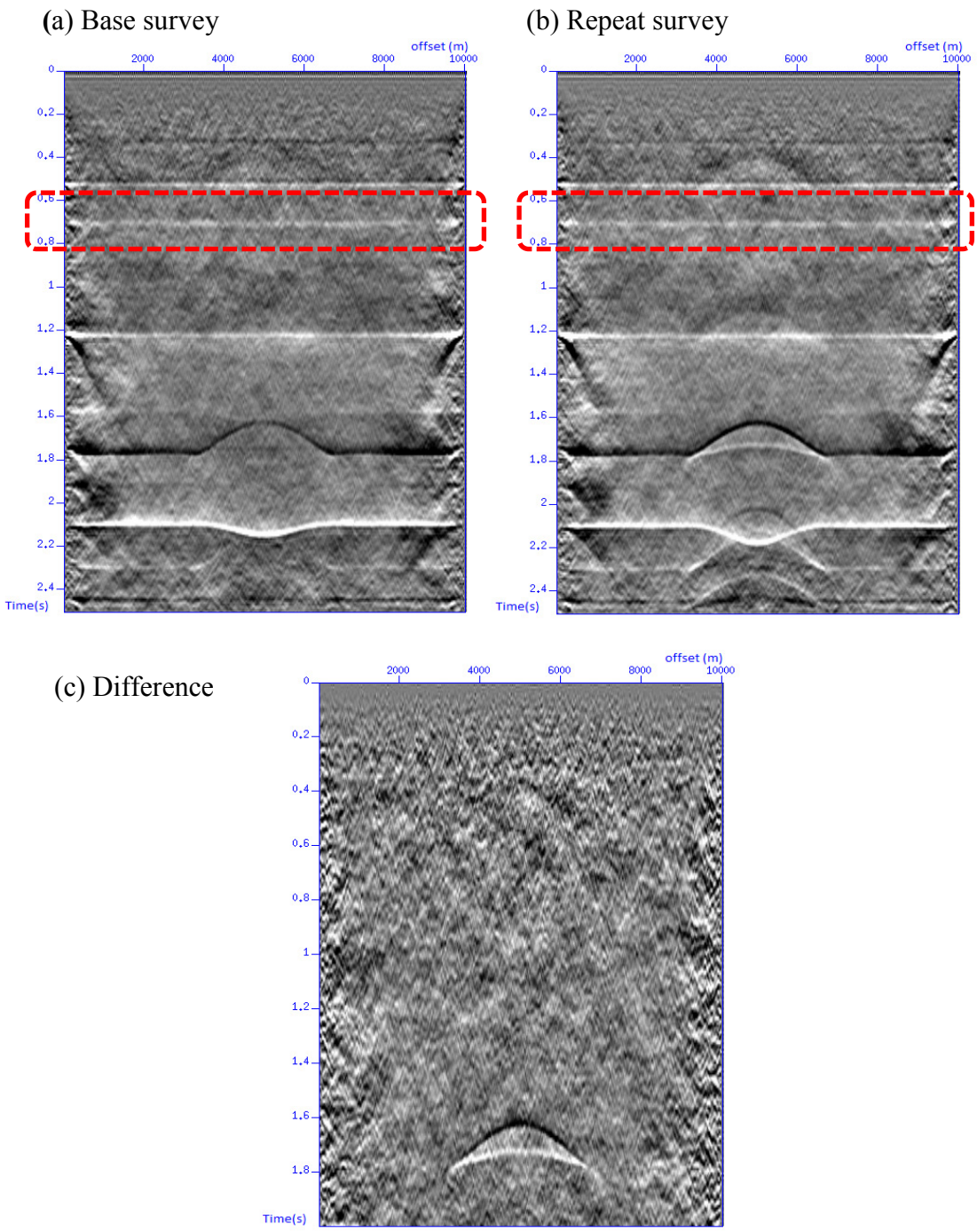

Figure 3.10. Stacked images from deconvolution method for the time lapse reservoir monitoring simulation. (a) The stacked section for the base survey before CO_2 injection. (b) Stacked section for the repeat survey after CO_2 injection. (c) The difference between the repeat and base survey. The artificial reflection around 0.7s is indicated inside the red dashed rectangular.

From the stacked images, a spurious multiple appears from the deconvolution and cross correlation methods marked by red dashed rectangular in Figures 3.9 and 3.10. Here for the purpose of mitigating the artifact layers, we investigate the regularization parameter (ε) which refers to the average amplitude spectrum recorded at the reference receiver and its effect on the quality of extracted response (Mehta and Graizer 2007; Nakata and Snieder 2012). Taking the simple impulsive source as an example, so the equations for the three methods are

$$C_{AB} = G(r_A, s)G^*(r_B, s) \tag{16}$$

$$D_{AB} = \frac{G(r_A, s)G^*(r_B, s)}{|G(r_B, s)|^2 + \varepsilon} \tag{17}$$

$$D_{BA} = \frac{G(r_B, s)G^*(r_A, s)}{|G(r_A, s)|^2 + \varepsilon} \tag{18}$$

$$H_{AB} = \frac{G(r_A, s)G^*(r_B, s)}{|G(r_A, s)||G(r_B, s)| + \varepsilon} \tag{19}$$

The cross correlation and cross-coherence equations are symmetrical, so it does not affect the result of the retrieved response when A and B are exchanged. In contrast, the calculation of deconvolution is asymmetrical. Due to the positioning and sensitivity of receivers in practice, the amplitudes of the recorded data might vary trace by trace (Nakata and Snieder, 2011). Assume that the amplitude of the signal recorded at receiver A is represented by $u(x_A, s) = G(r_A, s)$ as the average amplitude of all receivers, while an anomaly of large amplitude $G(r_B, s)$ is recorded at receiver B where $G(r_B, s) = \alpha G(r_A, s)$ and $\alpha \gg 1$. Applying this to Eq (17) and Eq (18), we see that the amplitude

computed by deconvolution at Receiver A and B is the average amplitude multiplied by $1/\alpha$ and α respectively, which leads to a significant amplitude variation by trace. We just need to select a relatively small regularization parameter for cross coherence to avoid zeros of spectrum of the denominator because there is no significant amplitude variation to balance. By modifying the regularizations, the artifact layer is suppressed (Figure 3.11, 3.12).

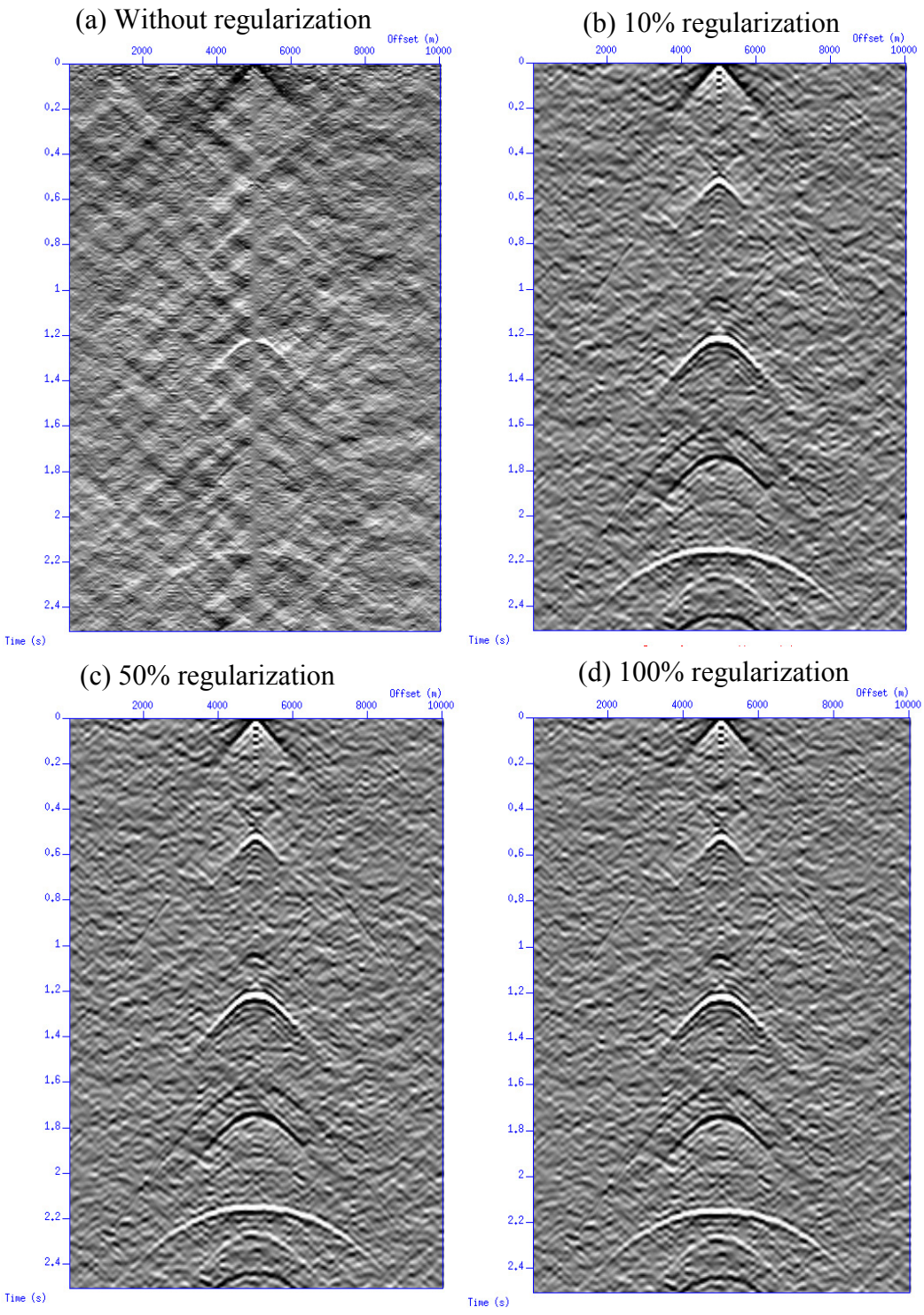

Figure 3.11. The regularization selection for deconvolution method. The instability caused by zeros of the spectrum of $u(r_A, s)$ and $u(r_B, s)$ is avoided. And the artefact layer is also suppressed. The regulation ε selected refers to the percent of the average spectral power of $u(r_B, s)$ in the denominator.

(a) Without regularization

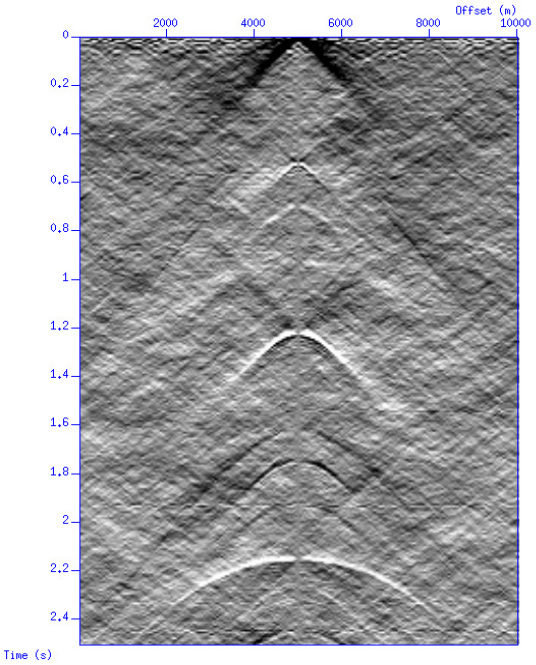

(b) 1% regularization

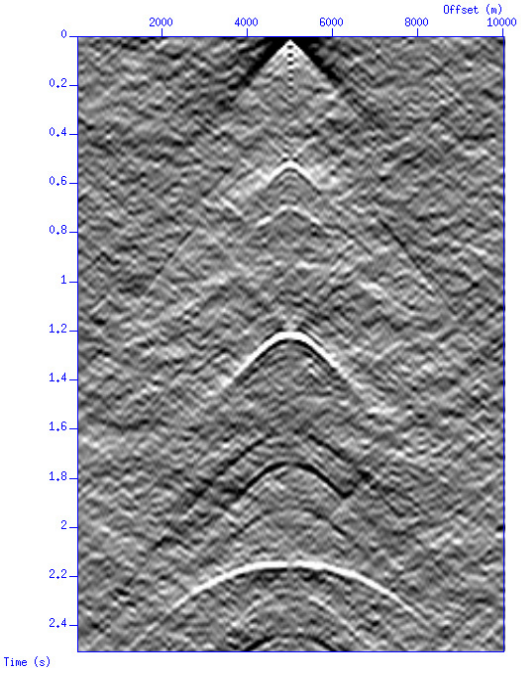

(c) 10% regularization

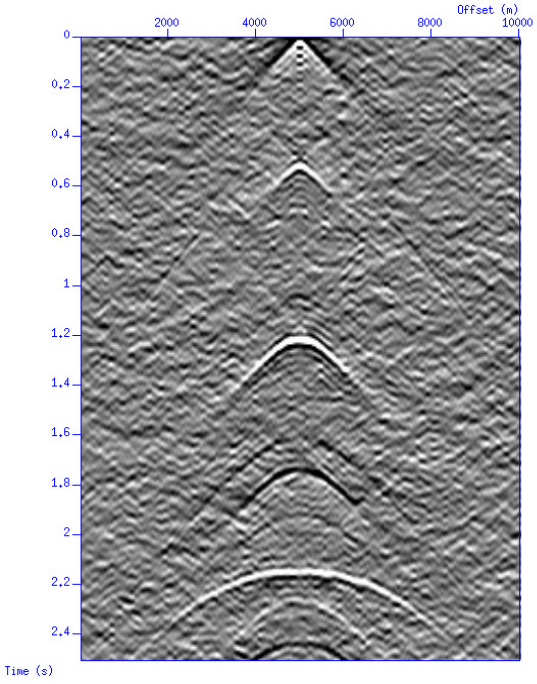

(d) 50% regularization

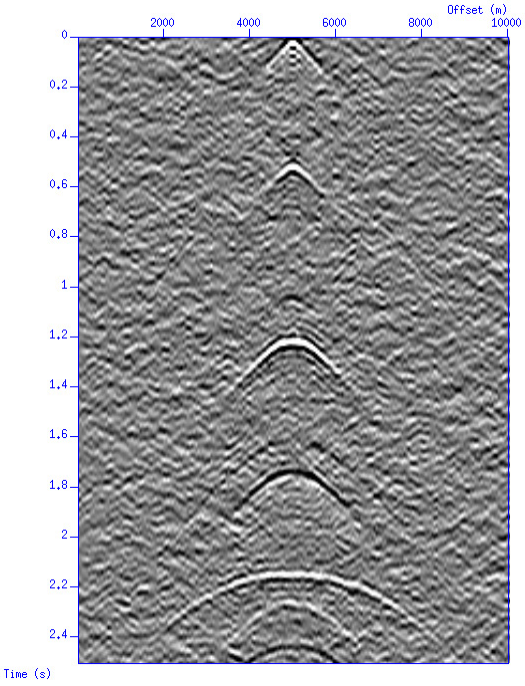

Figure 3.12. The regularization selection for cross coherence method. The artefact layer is removed. The regulation ε selected refers to the percent of the average spectral power of $u(r_B, s)$ in the denominator.

After we obtained reasonable regularization parameters for deconvolution and cross coherence, we generate new stacked images after applying regularization parameters to the recorded source signals and the time lapse difference owing to the impedance change over the top of the reservoir is calculated (Figures 3.13 and 3.14). The results of the stacked image and retrieved time lapse difference for the cross coherence and deconvolution methods are almost the same as that of the cross correlation method (Figure 3.8). Comparing the stacked image with and without any regularizations (Figures 13 and 9 for cross coherence, and Figures 14 and 10 for deconvolution), we see that the artifact response is suppressed.

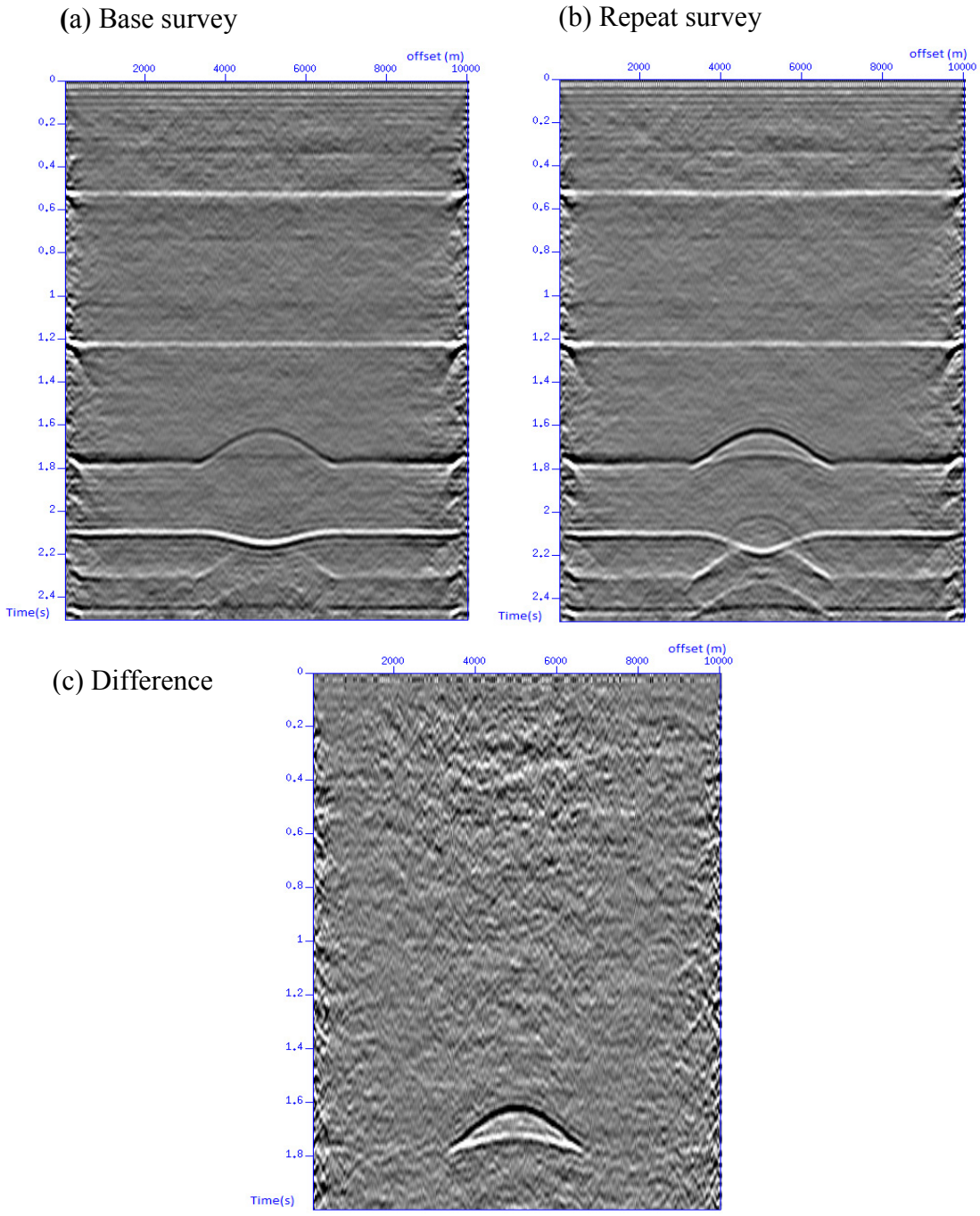

Figure 3.13. Stacked images from cross coherence method for the time lapse reservoir monitoring after applying regularization parameter. (a) The stacked section for the base survey before CO_2 injection. (b) Stacked section for the repeat survey after CO_2 injection. (c) The difference between the repeat and base survey. The artificial reflection around 0.7s is suppressed comparing with Figure 3.9a indicated inside a red dashed rectangular.

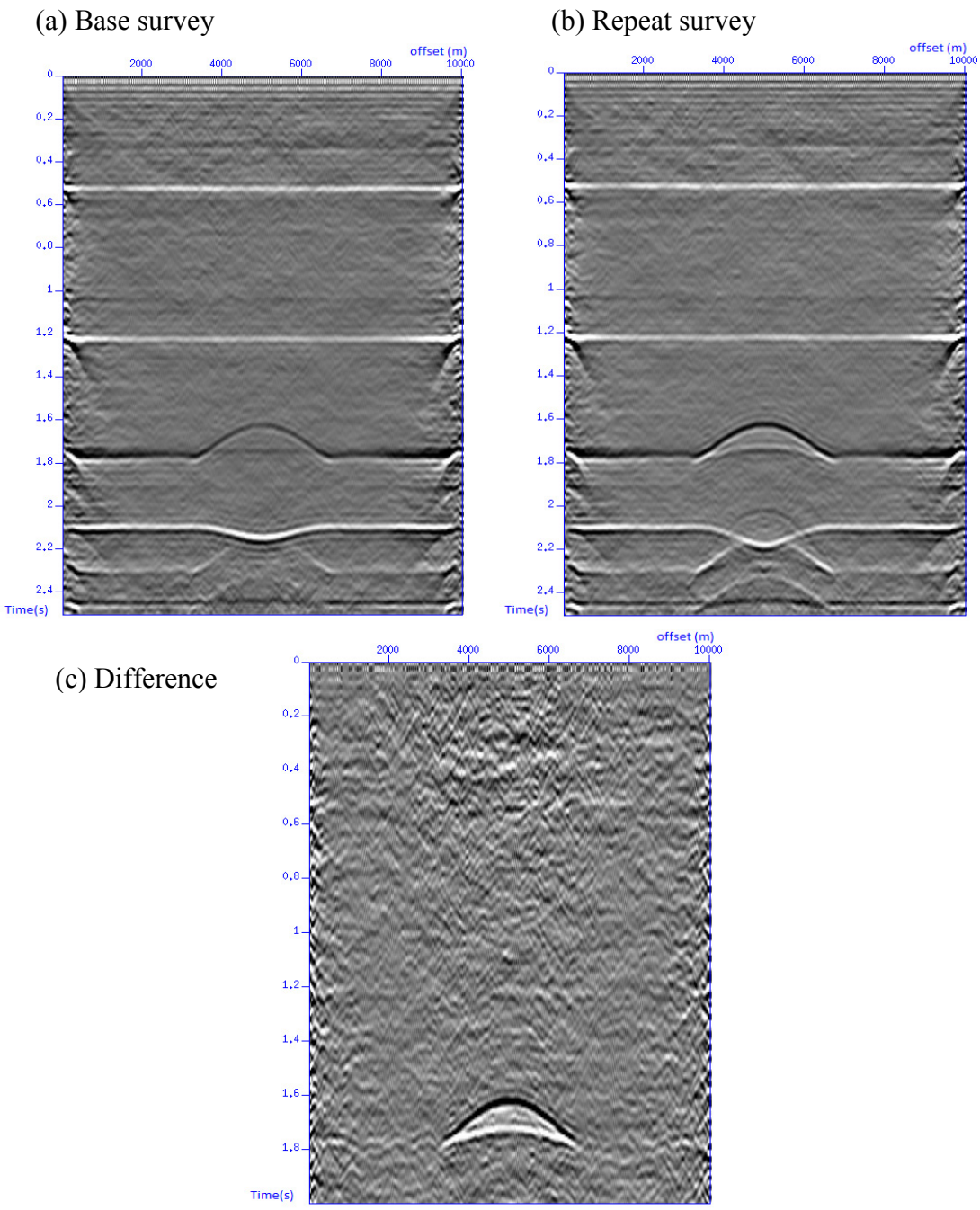

Figure 3.14. Stacked images from deconvolution method for the time lapse reservoir monitoring after applying regularization parameter. (a) The stacked section for the base survey before CO_2 injection. (b) Stacked section for the repeat survey after CO_2 injection. (c) The difference between the repeat and base survey. The artificial reflection around 0.7s is suppressed comparing with Figure 3.10a indicated inside a red dashed rectangular.

4. Signal to noise ratio analysis

4.1 Adding random noise with the same signal to noise ratio

In the chapter 3.4, we applied a regularization parameter to cross coherence and deconvolution methods for the time-lapse measurement in an optimal case without any random noise adding to the signal noise data. While the signal noise recorded in the deep formation is highly probably accompanied by random noise generated at the surface, to simulate the scenario in practice we create random noise with Gaussian distribution and add the random noise to the recoded signal noise. The probability density of the Gaussian distribution is

$$f(x|\mu,\sigma^2) = \frac{1}{\sqrt{2\sigma^2\pi}} e^{-\frac{(x-\mu)^2}{2\sigma^2}} \tag{21}$$

where x is the amplitude of the random noise amplitude and μ denotes the mean amplitude of the random noise and also the mean amplitude of the signal noise. σ^2 represents standard deviation of the random noise. The signal to noise ratio (SNR) is calculated by

$$SRN = \frac{\sigma_{signal}^2}{\sigma_{noise}^2} \tag{22}$$

where σ_{signal}^2 and σ_{noise}^2 are the standard deviation of the recorded signal noise and random noise respectively.

Given the mean amplitude and standard deviation of the signal noise for the total 201 traces, the random noise data is generated based on the equation (19) and (20) with signal to noise ratio of 0.5 and 1. Summing the random noise to the signal noise with the

different SNR of 0.5 and 1, the stacked image produced by cross correlation, deconvolution and cross coherence are compared (Figure 4.1, 4.2).

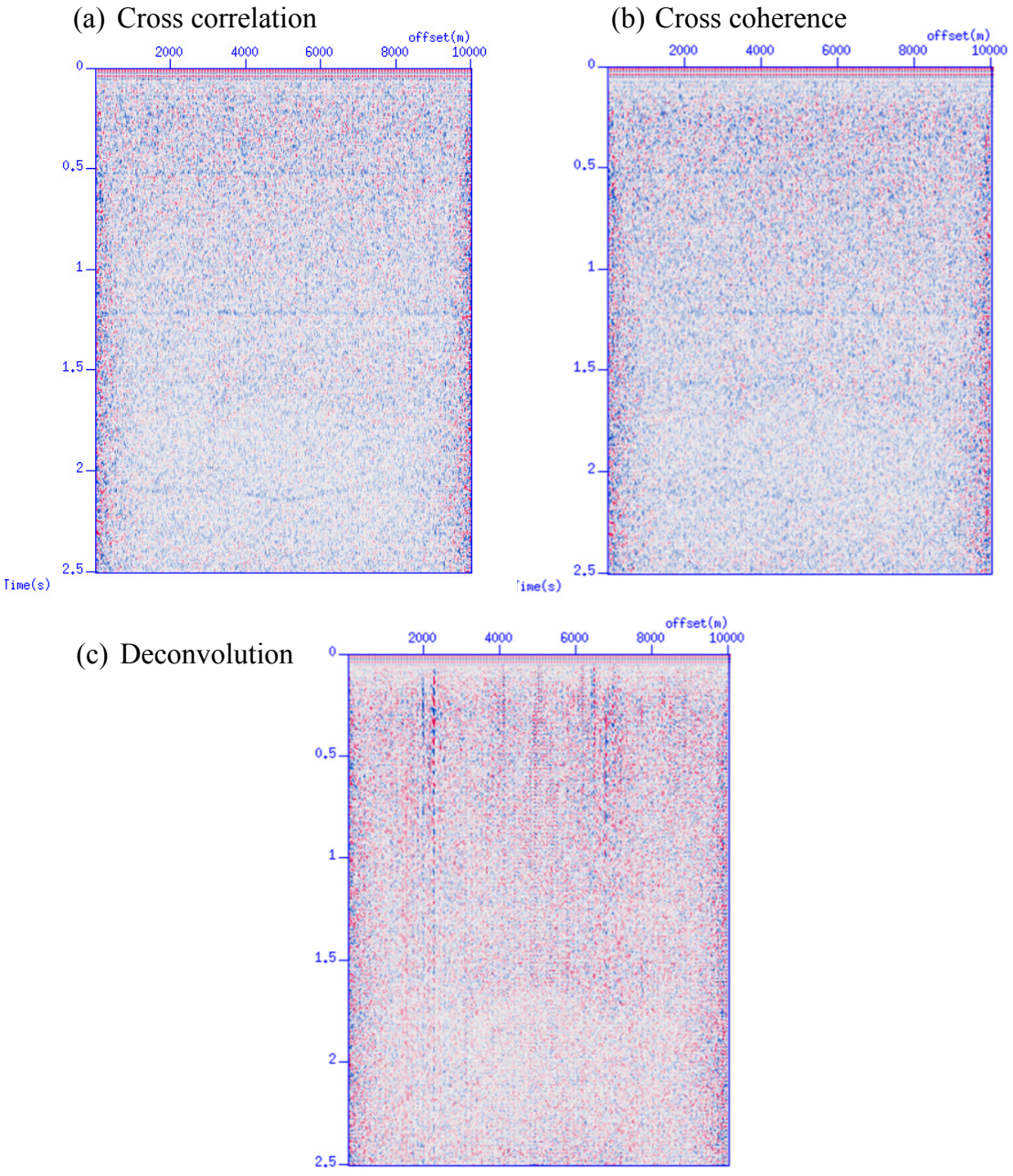

Figure 4.1. The post stack image of the first 2.5s data by cross correlation, cross coherence and deconvolution methods. The source to signal ratio equals to 0.5.

(a) Cross correlation

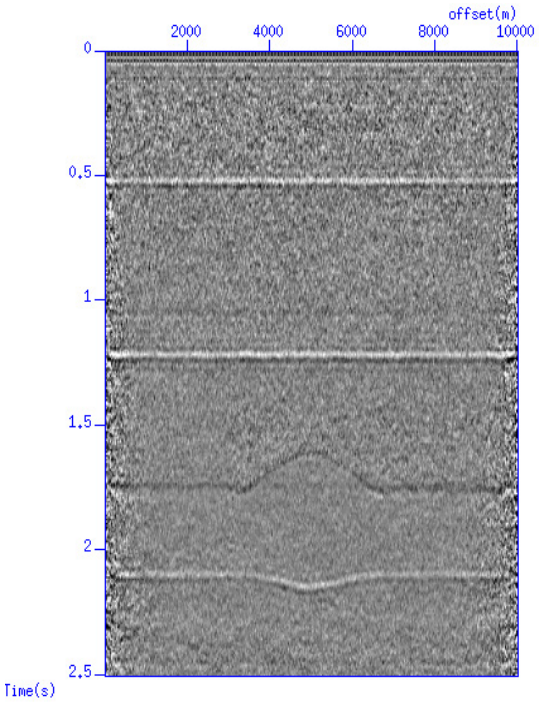

(b) Cross coherence

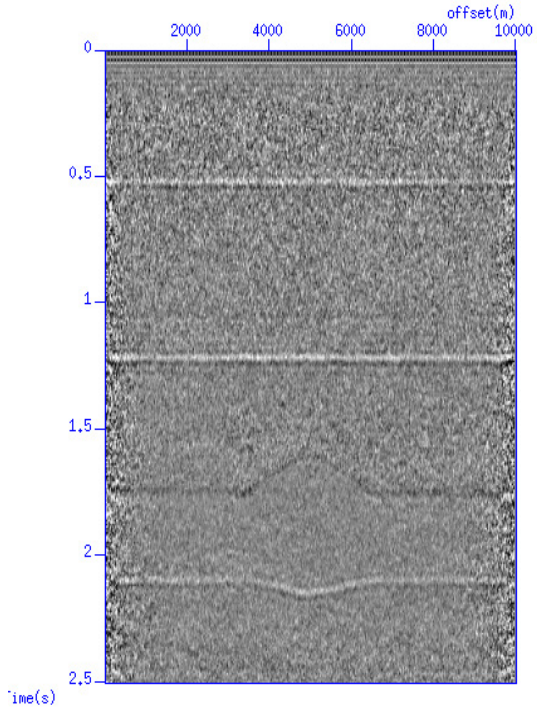

(c) Deconvolution

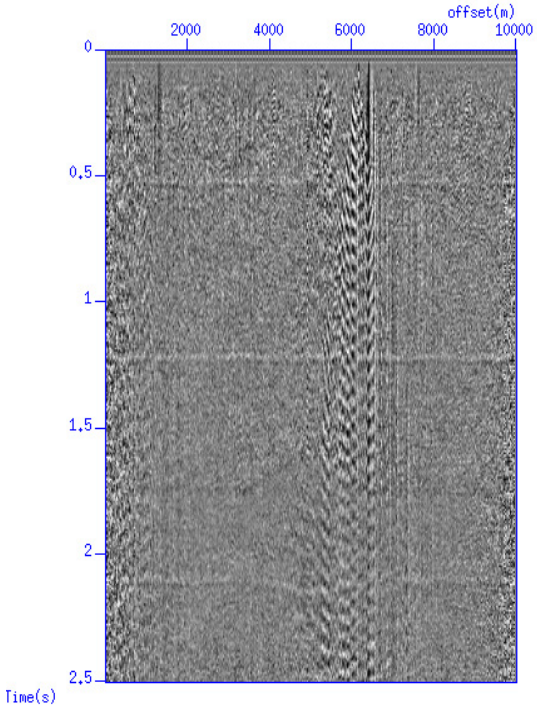

Figure 4.2. The post stack image of the first 2.5s data by cross correlation, cross coherence and deconvolution methods. The source to signal ratio equals to 1.

From Figure 4.1 and Figure 4.2 we can see that there is no obvious difference between the stacked images generated by cross correlation and cross coherence. In contrast, because no additional regularization parameter is applied, the deconvolution method shows its inherent instability caused by amplitude variation between traces.

4.2 Adding random noise with different signal to noise ratio

To make the signal to noise ratio model in section 4.1 more practically when taking the equipment positioning and overlap of interfering waves into account, the anomalous amplitude traces might occur at random receiver positions. As a result the model can be improved by changing from the same SNR of all traces into different SNR to different traces. The modeled SNR at difference traces from 0.1 to 0.5 and 0.01 to 1 is randomly selected. The random SNR for each of the 201 traces we applied is shown in Figure 4.3.

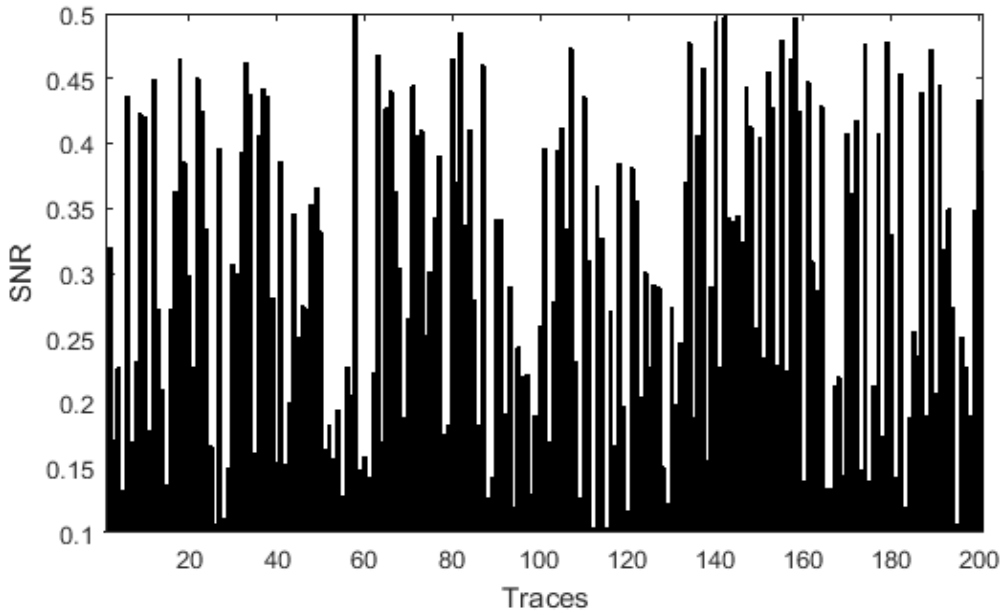

Figure 4.3. The random signal to noise ratio between 0.1 and 0.5 modeled at the 201 traces.

We choose one recorded signal noise and the modeled random noise at the location of receiver 101 for display (Figure4.4). The SNR of the selected trace is 0.3941.

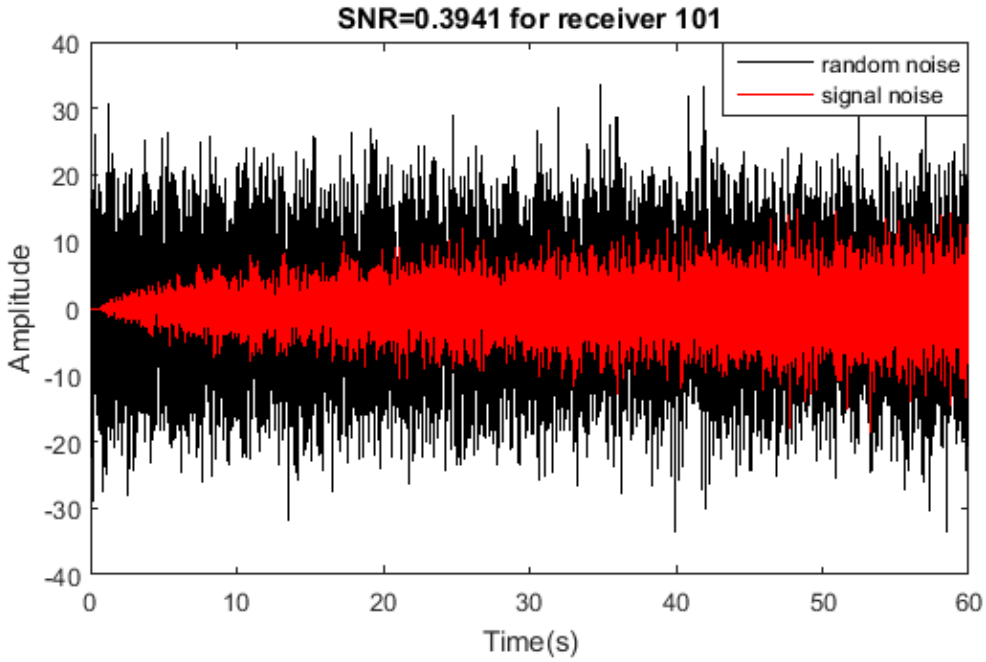

Figure 4.4. The red line is the recorded signal noise from the deep formation and the black line represents modeled random noise at the location of receiver 101. The signal to noise ratio for the trace 101 is 0.3941 which is a random number between 0.1 and 0.5.

Figure 4.5 compares the stacked images of seismic interferometry generated by cross correlation, deconvolution and cross coherence methods. Cross correlation generates much more incoherent noise, and the reflections retrieved by deconvolution is less virtually obvious. Cross coherence shows its advantage and generates the most coherent reflections.

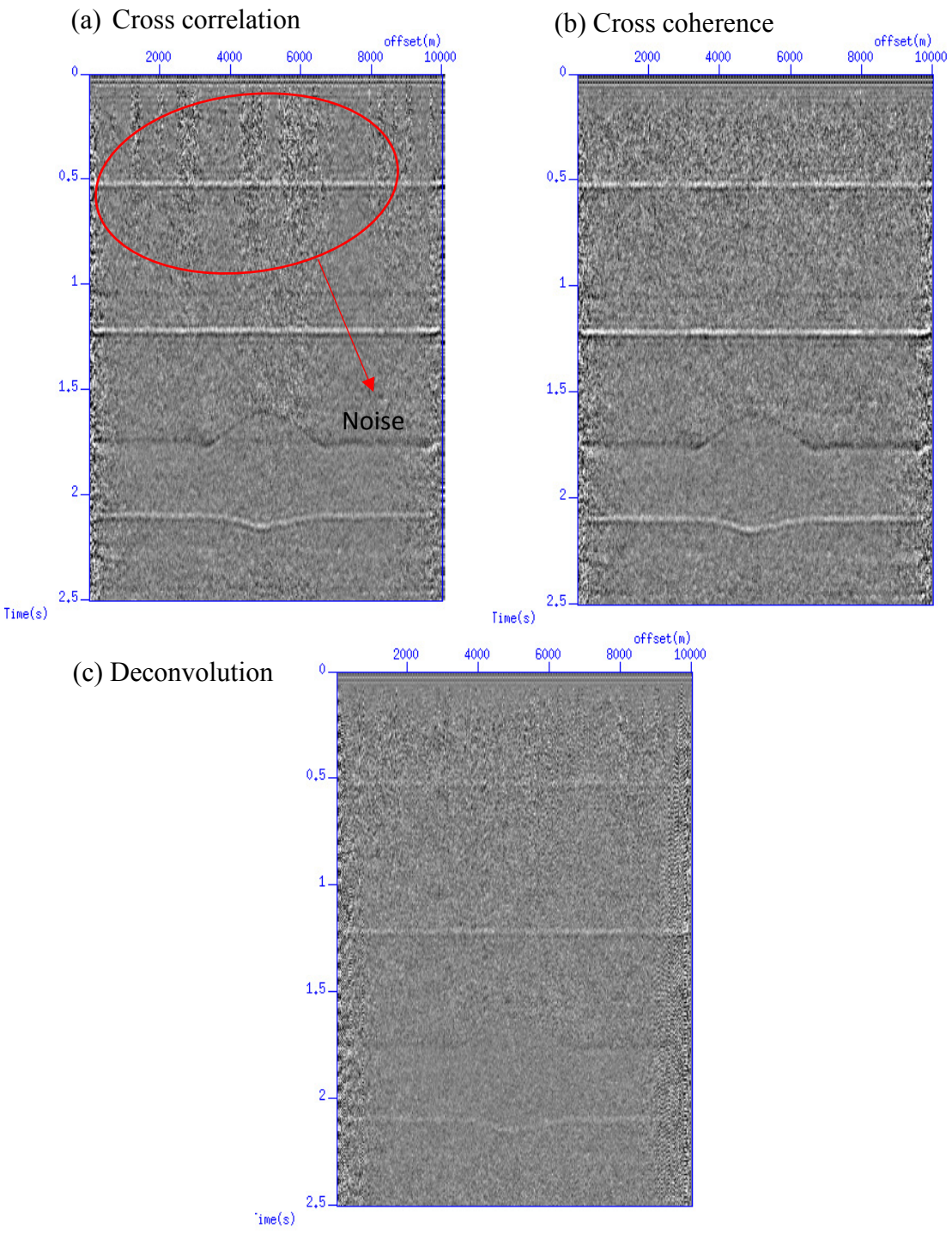

Figure 4.5. The stacked image of seismic interferometry produced by cross correlation, deconvolution and cross coherence from traces with signal to noise ratio from 0.1 to 0.5 (a) Cross correlation method shows more incoherent noise marked by red ellipse.

We then change the signal to noise ratio for each traces from 0.1 - 0.5 to 0.01 – 1 to investigate the influence of the variation of the SNR of different traces on the seismic interferometry reflection wave retrieval. Figure 4.6 shows the random SNR from 0.01 to 1 for each of the 201 recorded noise and Figure 4.7 demonstrates one trace of signal noise and random noise recorded at the location of receiver 101. Figure 4.8 compares the stacked image generated by cross correlation, deconvolution and cross correlation.

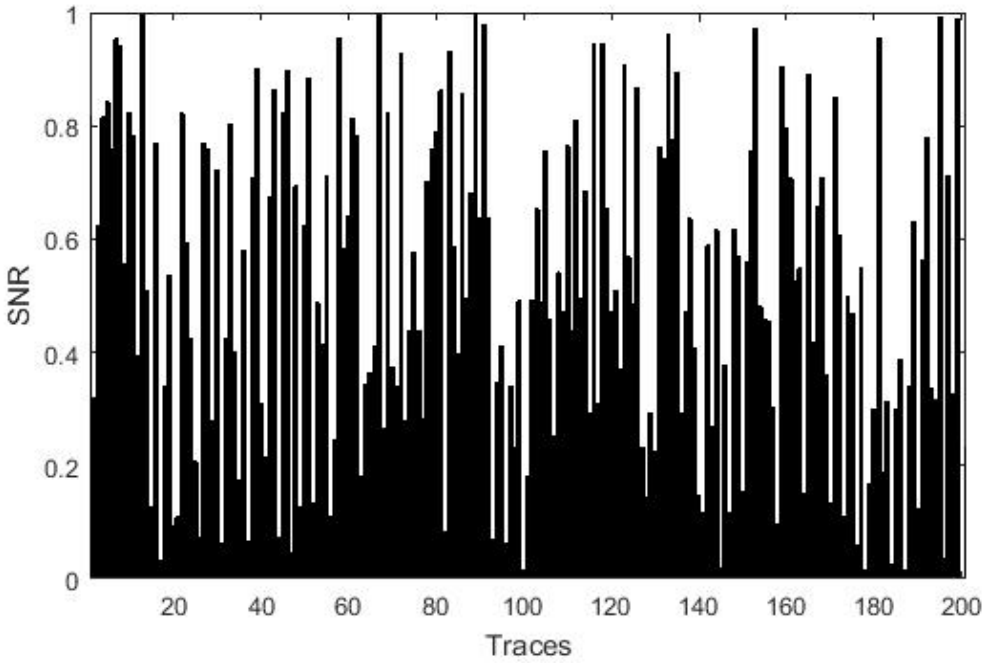

Figure 4.6. The signal to noise ratio from 0.01 to 1 for 201 traces

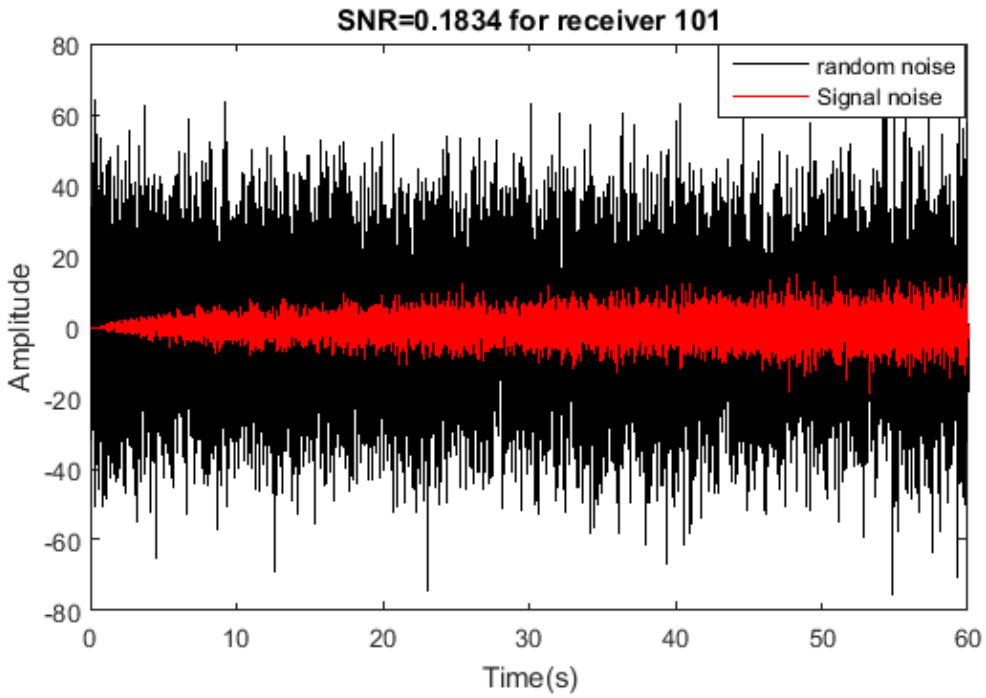

Figure 4.7. One trace of recorded signal noise in red line and random noise in black line at the location of receiver 101. The signal to noise ratio of trace 101 is 0.1843.

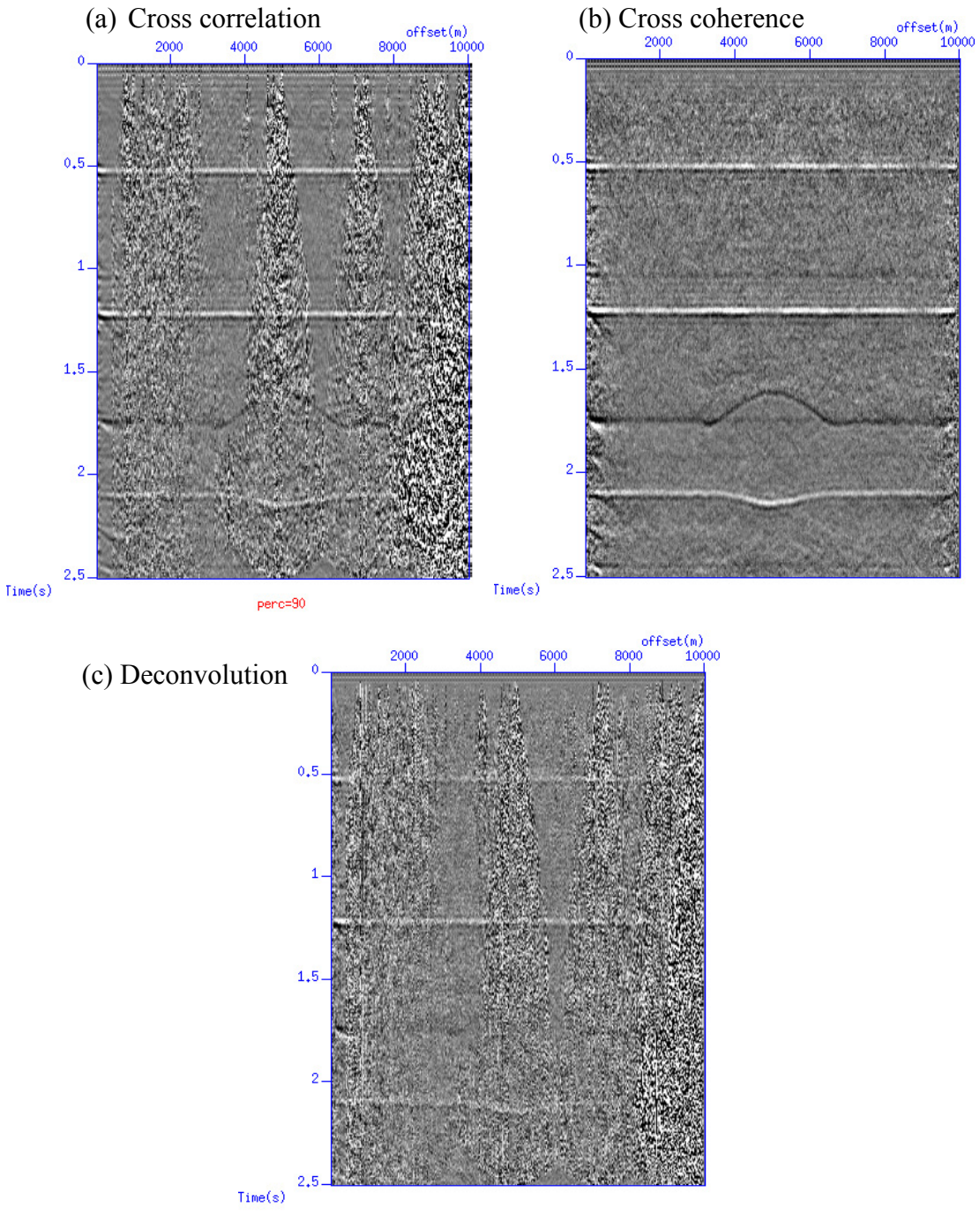

Figure 4.8. The stacked image of seismic interferometry produced by cross correlation, deconvolution and cross coherence from traces with signal to noise ratio from 0.01 to 1. Much more incoherent noise appears in cross correlation (a) and deconvolution (b) methods.

5. Source noise frequency analysis

Low frequency seismic waves are usually recorded with contamination of noise that will affect the resolution of the retrieved reflections. In section 2 we have already presented the equations (11, 12, and 13) for the cross correlation, deconvolution and cross coherence methods and discussed the properties of the three methods. The deconvolution and cross coherence methods are independent of source signature, because the wavelet $W(s)$ is cancelled from the denominator and numerator. Figure 5.1 compares the stacked images processed by the three methods from source noises with maximum 5Hz frequency. From Figure 5.1 it is clear that the temporal resolution of the stacked images generated by deconvolution of cross coherence is much higher than that of cross correlation.

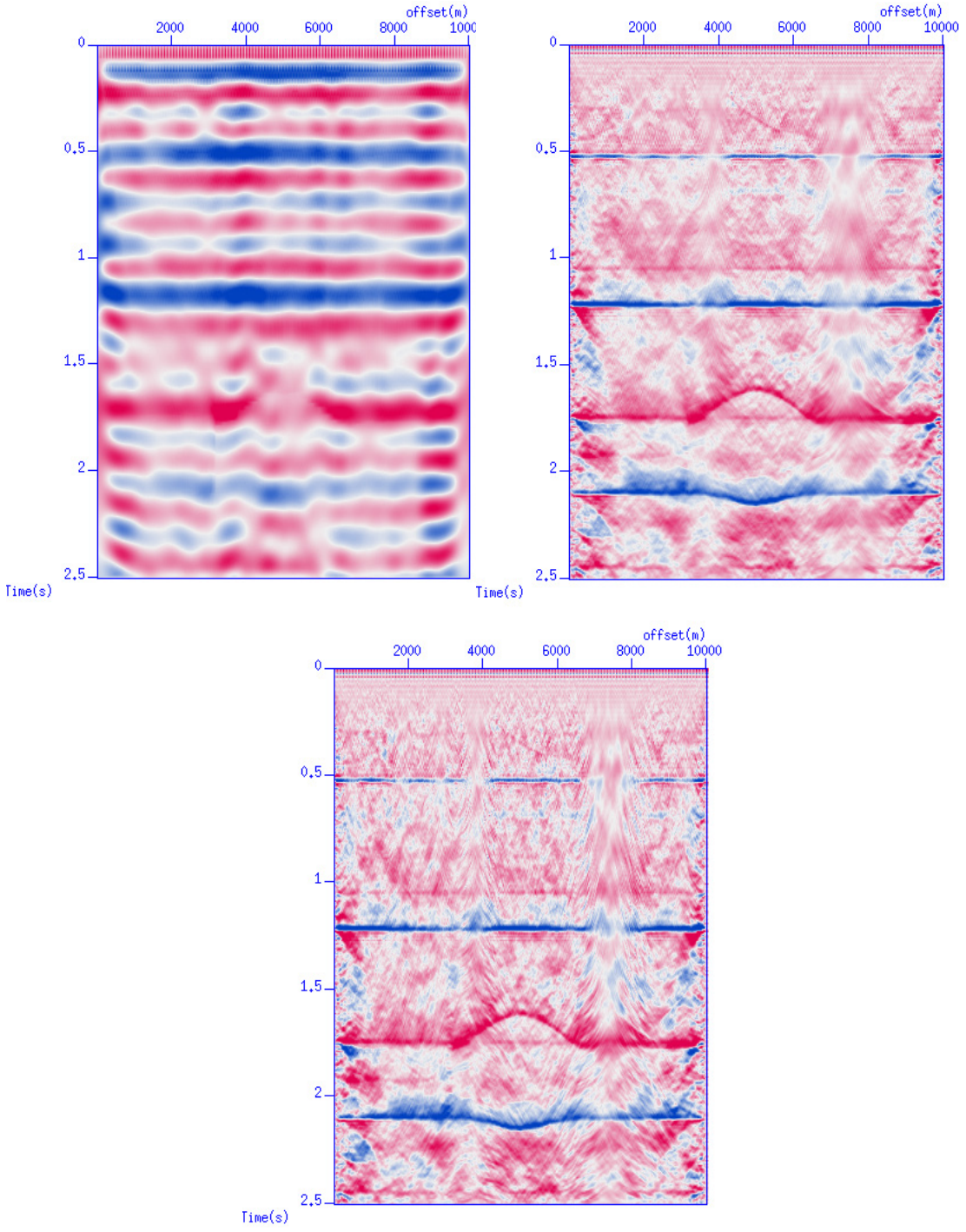

Figure 5.1. The stacked image of seismic interferometry produced by cross correlation, deconvolution and cross coherence. The maximum frequency of source noises recorded from the deep formation is 5Hz.

6. Application to field data

6.1 Passive seismic data description

We now apply the methods to real data from the field. The noise data was collected at the Ketzin, Germany, CO_2 storage site in 2011 February (Frster et al., 2006). The noise sources are comprised of natural earthquakes, wind and vehicles, and other typical sources. The data consists of 63 traces with a geophone interval of 24 m and recording time of 28.7 hours. Accordingly, it includes 3448 separate "panels" with recording times of 30s each. The sample rate is 4ms and each panel has 63 traces corresponding to the 63 geophones. The data examined by previous research (Xu et al., 2012) indicates that the frequency band between 2 to 30 Hz contains the most useful information and that the frequency band between 14 to 28 Hz possesses mainly the body waves. Unfortunately, in most of the noise panels, deeper reflectors could not be imaged due to the insufficient signal to noise ratio (Xu et al., 2012).

6.2 Pre-processing

With respect to the anomalous amplitude of some traces in one panel's recording, pre-processing need to be performed before cross correlation, deconvolution and cross coherence. The raw data for one noise panel is shown in Figure 6.1 from which we can identify traces with anomalously high amplitude; we conclude that the amplitude is not balanced between traces. I tested multiple trace normalization methods including normalization by subtracting the median and maximum amplitudes of each traces and normalization by subtracting root mean square (RMS) amplitude of each trace Eq (20). The RMS normalization method was selected and is applied trace by trace to ensure that

all the traces are equally weighted. After the normalization, we inspect the frequency content of the traces and obtain the frequency spectrum from one panel's noise recording (Figure 6.2). Frequency is on the vertical axis and trace number is on the horizontal. The main energy is concentrated between 2 and 38 Hz and a bandpass filter between 2 and 30Hz is applied. The recorded noise of one panel after normalization and bandpass filter is presented in Figure 6.3.

$$x_{rms} = \sqrt{\frac{1}{n}(x_1^2 + x_2^2 + \cdots + x_n^2)} \qquad (20)$$

Although I applied normalization by RMS, if additional pre-processing work is applied, such as sign-bit normalization (Xu et al., 2012), the result of cross-correlation might be improved. The sign bit normalization potentially, however, removes the information on the relative amplitude of the reconstructed signals (Larose, 2006; Larose et al., 2007).

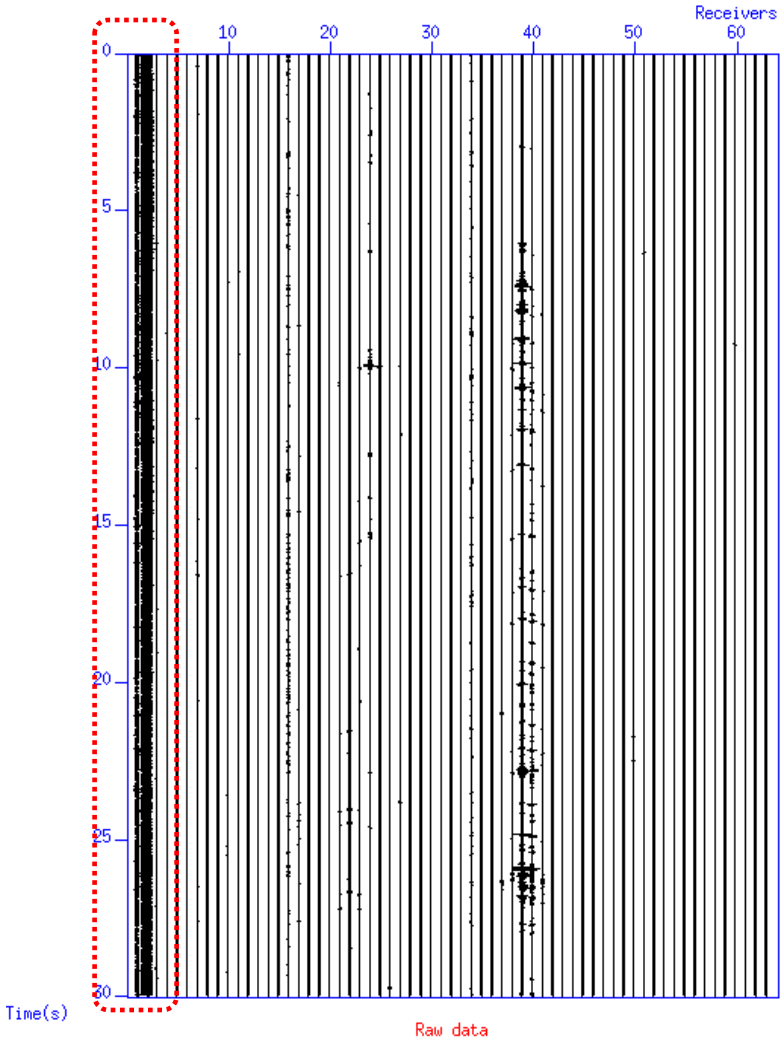

Figure 6.1. The raw data of 63 traces from only one time panel. The traces of anomaly amplitude are marked by red dashed rectangular.

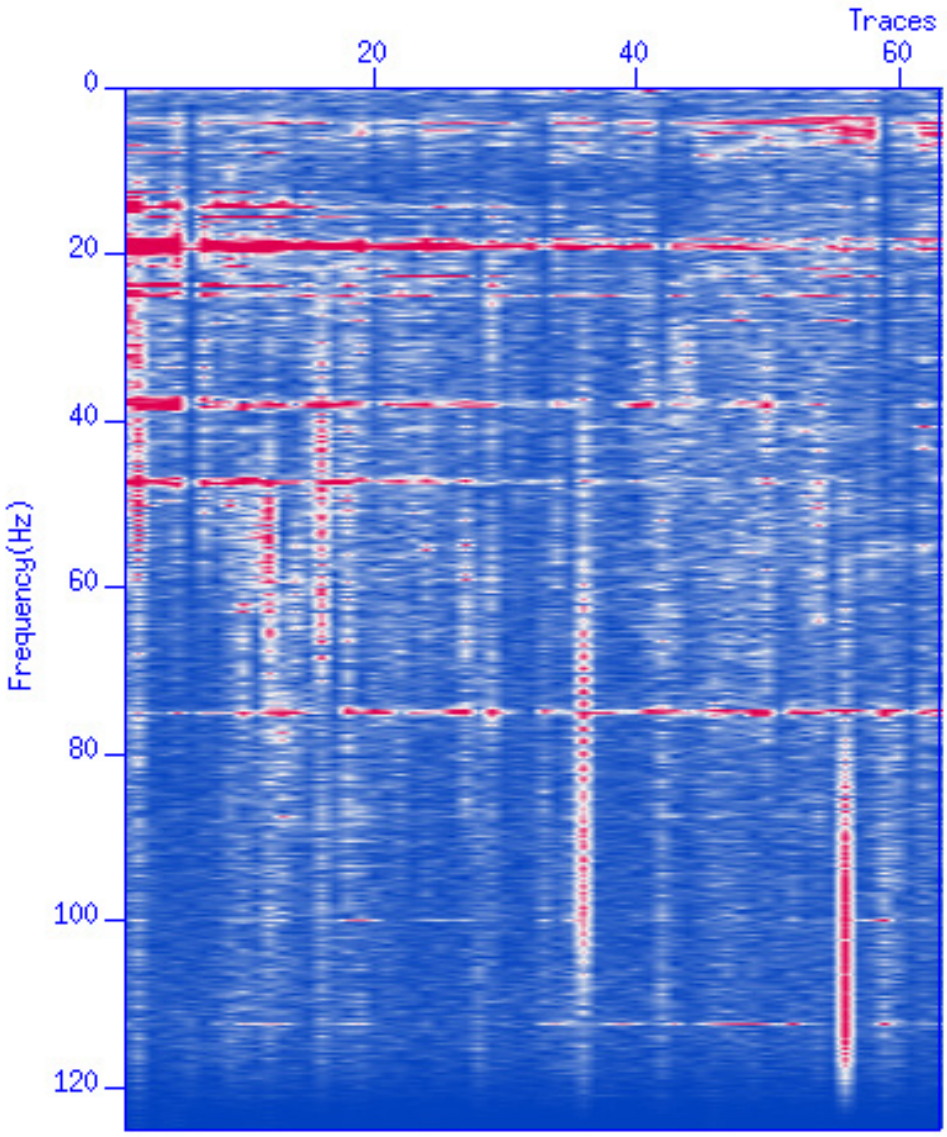

Figure 6.2. The frequency spectrum of the noise data from panel 3500. The energy is mainly concentrated between 2 and 38Hz.

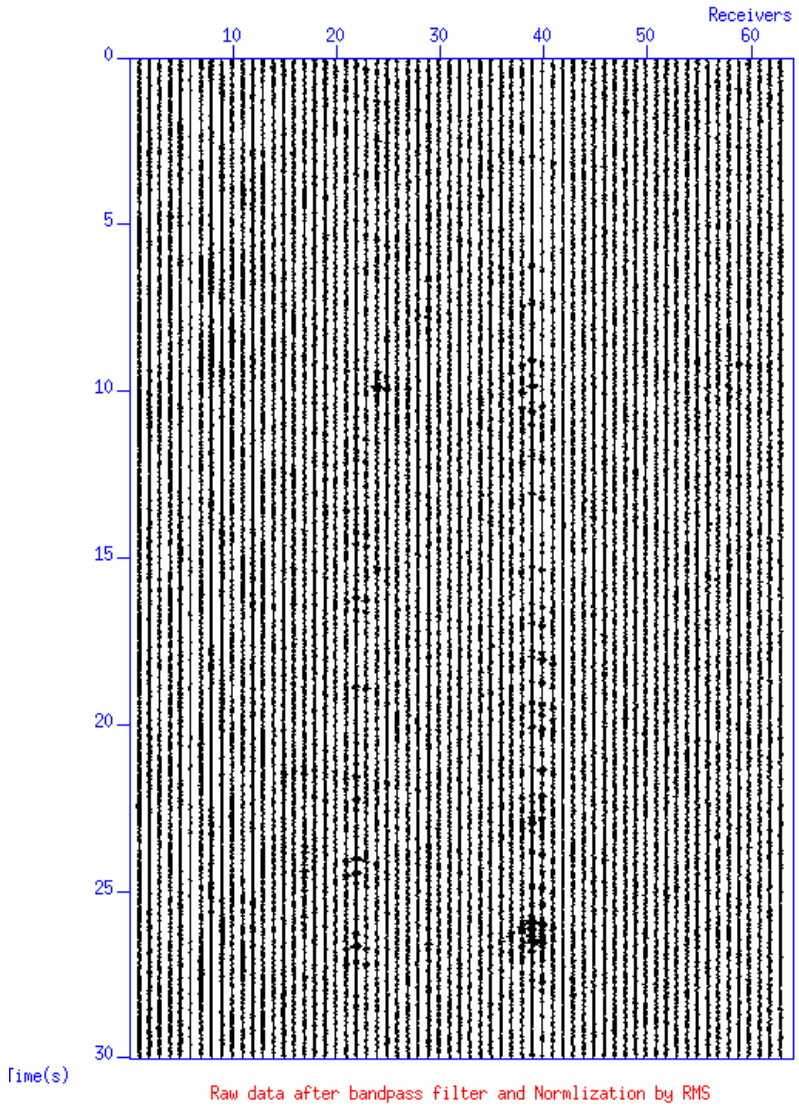

Figure 6.3. The noise signal data normalized by RMS method for one panel. The traces of anomaly amplitude is balanced.

6.3 Seismic response retrieval for field data

Because the noise data was only recorded after CO_2 injection, a comparison of the base and repeat passive seismic survey is not possible. Therefore, in this field data case study, we only focus on the comparison of retrieved seismic obtained from cross correlation, deconvolution and cross correlation. Also due to the limited recording time of dataset, thereby, we do not expect to obtain a perfect seismic image, but have sufficient data to compare the three methods for seismic response retrieval.

Figure 6.4 shows the cross correlation result for just one panel from which the retrieved seismic response is not identifiable, apparently because of a very low signal to noise ratio. Therefore, we apply the cross correlation to each of the 3448 panels and then stack the 3448 outputs together to enhance the signal to noise ratio (Figure 6.5). From Figure 6.5 the steeply dipping straight-line events represent ground roll and the flatter events are body waves. In order to keep only the body waves that we are interested in, a band pass filter between 14 and 26 Hz is applied to remove the lower-frequency surface waves. Figure 6.6 shows the filtered body waves.

Because there is overlapping frequency content between the surface waves and body waves, we applied an *f-k* filter to suppress the surface wave and direct waves. The seismic response of the reflected body waves is enhanced. The same workflow to process the data is also applied for deconvolution and cross coherence method for comparison. Figure 6.7 exhibits the result of deconvolution and cross coherence after applying the *f-k* filter. Due to the computation power and calculation time for virtual common shot gathers at each of the location of receivers, only one common shot gather at the position of receiver 30 is generated for display. Therefore, sorting the common shot gathers to CMP gathers or

common offset stack gathers which will further improve the signal to noise ratio cannot be implemented in my study. The reflection event cannot be extracted from a common shot gather.

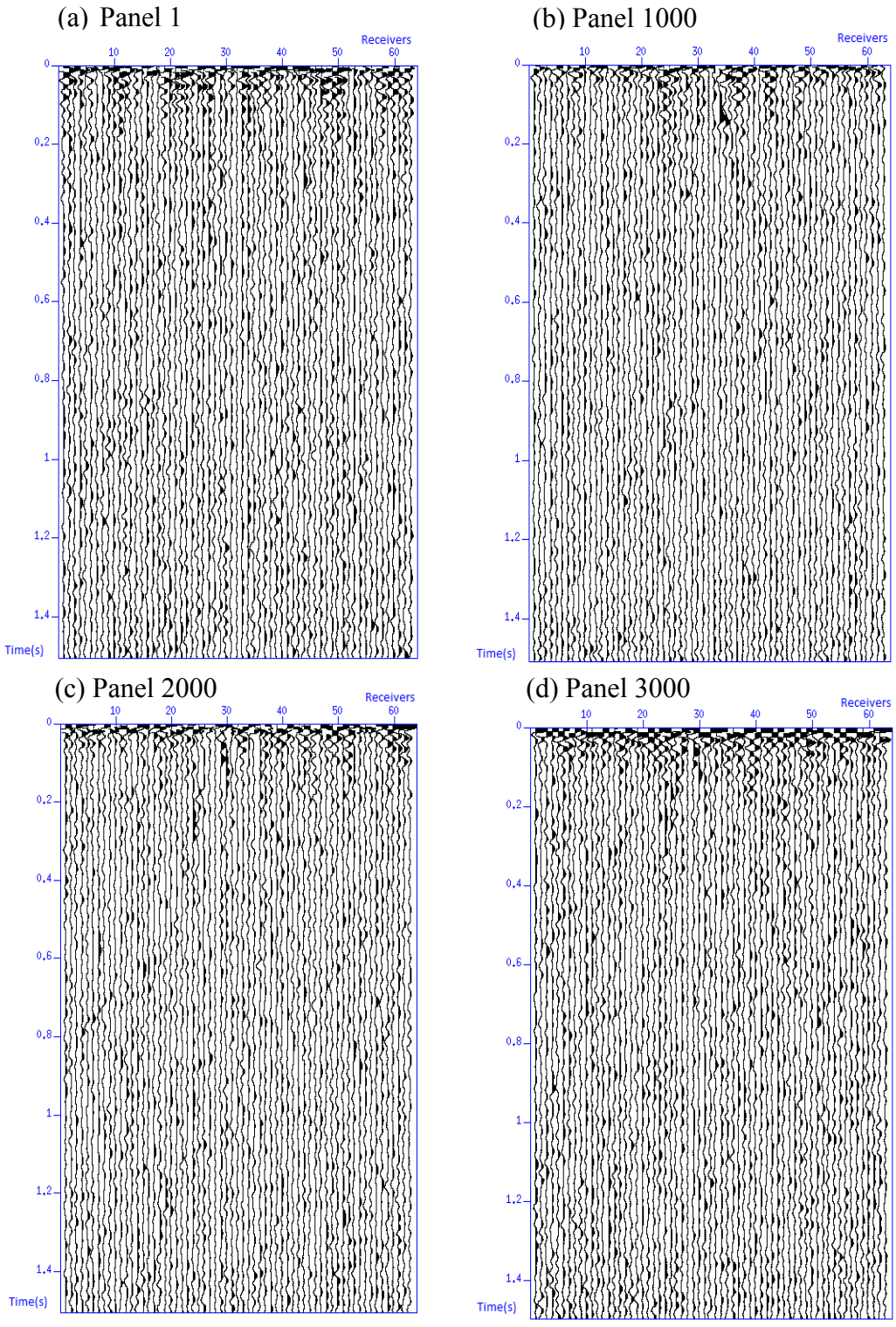

Figure 6.4. Panel 1, Panel 1000, Panel 2000 and Panel 3000 after cross correlation are selected for display the low signal to noise ratio. Either the surface wave or body wave are not identifiable.

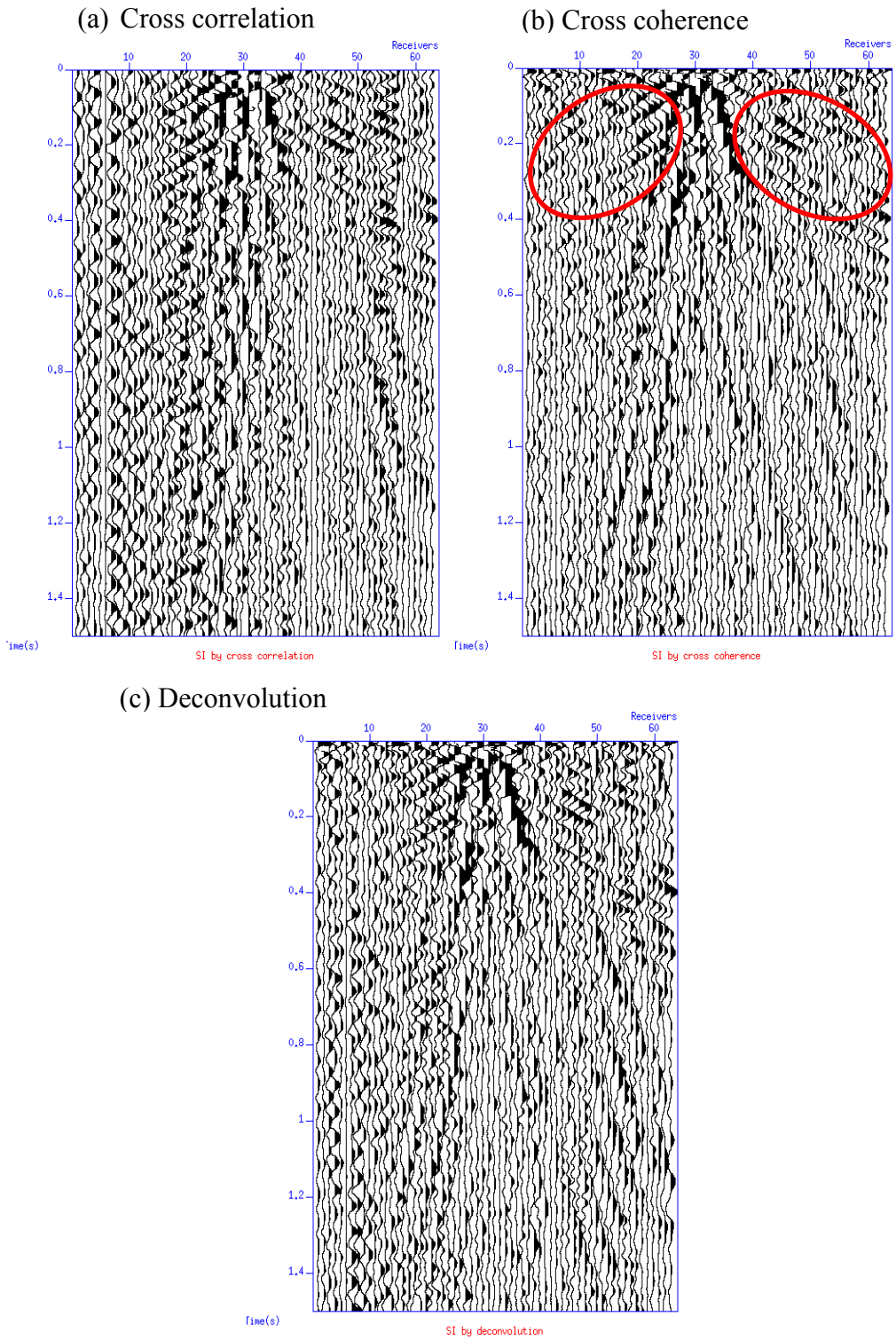

Figure 6.5. The virtual common shot gathers retrieved at location of receiver 30 by cross correlation, cross coherence and deconvolution methods after summing all the 3348 panels. The body waves are indicated by red ellipses in (c).

(a) Cross correlation

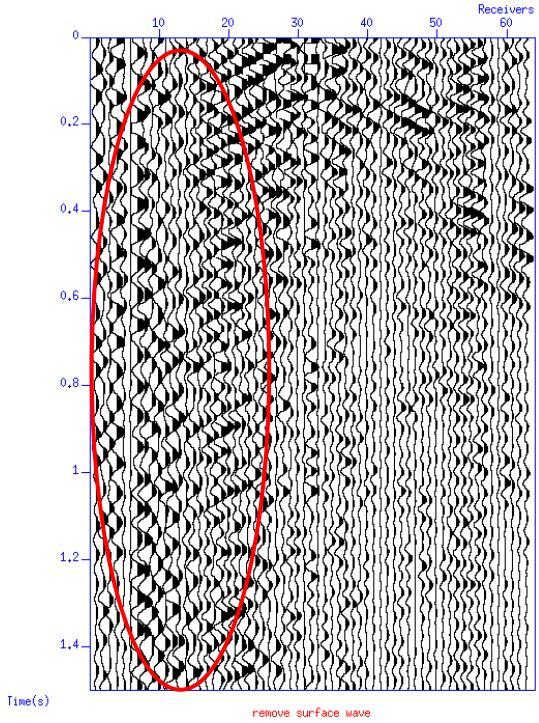

(b) Cross coherence

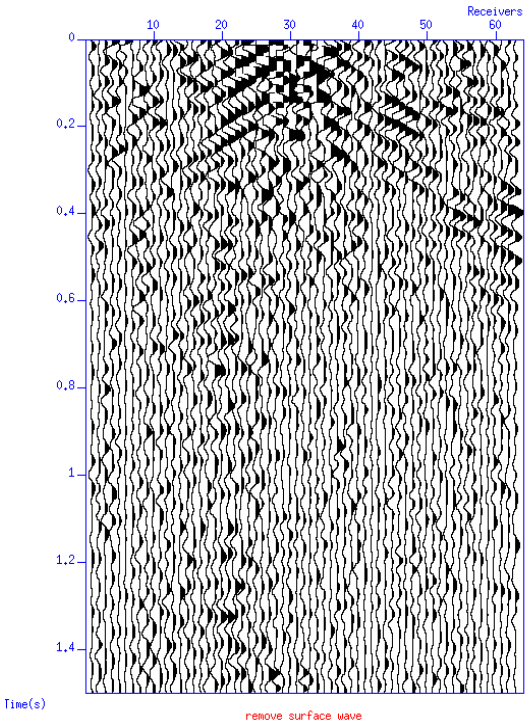

(c) Deconvolution

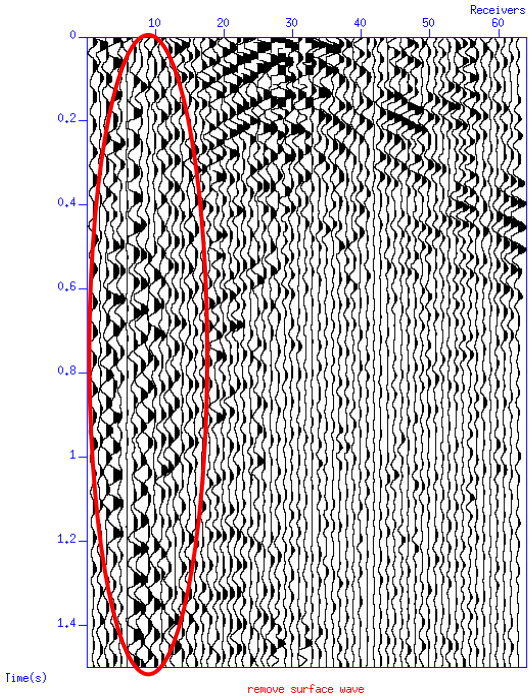

Figure 6.6. The band passed filter between 14-26HZ is applied to extract body waves for the data of Figure 6.5. Traces of anomaly amplitude still exist for cross correlation and deconvolution method indicted in the red ellipses.

a) Cross correlation

b) Cross coherence

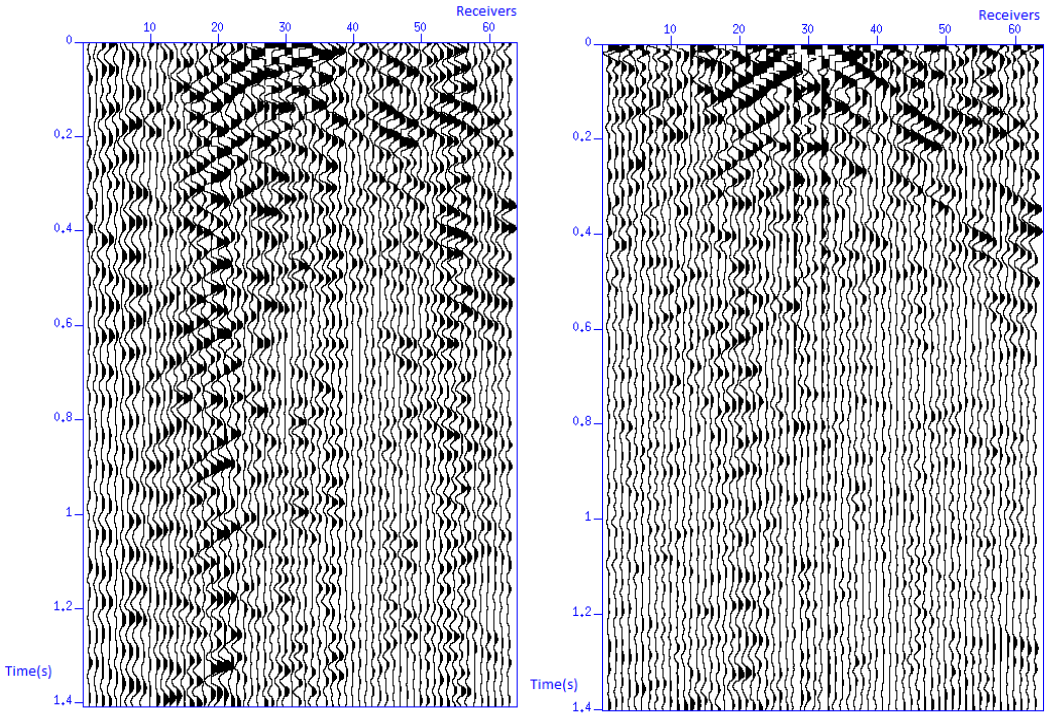

c) Deconvolution

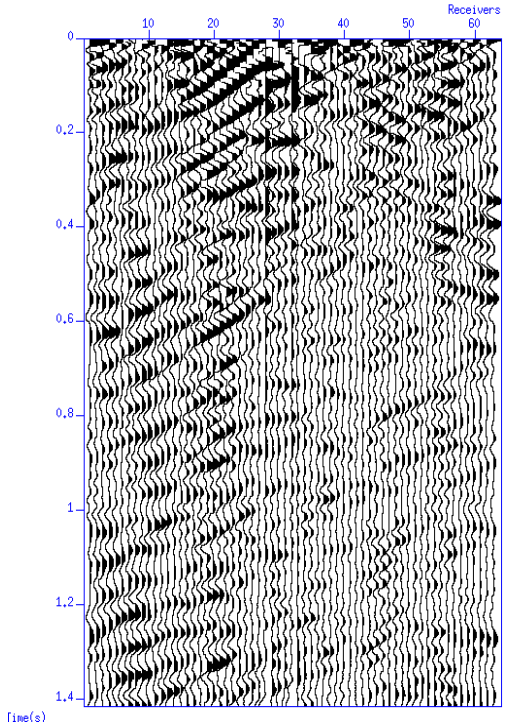

Figure 6.7. The FK domain filter is applied to extract body waves for the data of Figure 6.5.

7. Conclusion

From the synthetic data modeling result, seismic interferometry shows the potential to be a useful technique for time lapse monitoring, one that is cost effective and environmentally friendly compared to conventional active-seismic time lapse surveys. This study compared three methods of processing the noise data. Of those, it seems from visual inspection of synthetic data analysis that the cross coherence method is better than the cross correlation or deconvolution methods. While the cross coherence and deconvolution method will potentially generate artifact reflections. The regularization parameter to control the stability of cross coherence and deconvolution is studied. We observe that the artifact reflections could be removed by adding an appropriate regularization parameter. Whereas, the regularization parameter should be chose carefully. If the selected regularization is too small, deconvolution and cross coherence are not stable; if the regularization is too larger cross correlation and deconvolution would reduce to cross correlation.

In addition, to make the synthetic model more realistic, adding random noise to signal noise and low frequency case are investigated. Cross correlation and cross coherence methods generate similar stacked images using random noise with a same signal to noise ratio to all traces. Whereas, cross coherence works best using random signal to noise ratios to different traces. Moreover, in constrained low frequency model, cross coherence and deconvolution produce better temporal resolution comparing with that of cross correlation because cross coherence and deconvolution are independent of noise source signature.

In the field data case, surface and body waves are retrieved and distinguished by bandpass and *fk* filter. Although the reflections is still not identifiable from a single virtual common shot gather at one receiver, cross coherence seems to provide a better result for the field data collected in Ketzin. Cross coherence is suitable for noise data with anomalous amplitude variations and complex source wavelets among traces considering the difference between the optimal synthetic data and complex field data.

8. References

Bakulin A. and Calvert R. 2006. The virtual source method: Theory and case study. Geophysics 71, SI139–SI150.

Bakulin, A. & Calvert, R., 2004. Virtual source: new method for imaging and 4D belowcomplex overburden, in 74th Annual International Meeting, SEG, Expanded Abstracts, 2477–2480.

Bakulin, A., Mateeva, A., Mehta, K., Jorgensen, P., Ferrandis, J., Herhold, I.S. and Lopez, J., 2007. Virtual source applications to imaging and reservoir monitoring. The Leading Edge, 26(6), pp.732-740.

Cheraghi, S., Craven, J.A. and Bellefleur, G., 2015. Feasibility of virtual source reflection seismology using interferometry for mineral exploration: A test study in the Lalor Lake volcanogenic massive sulphide mining area, Manitoba, Canada. Geophysical Prospecting, 63(4), pp.833-848.

Claerbout, J.F., 1968. Synthesis of a layered medium from its acoustic transmission response. Geophysics, 33(2), pp.264-269.

Draganov, D., Campman, X., Thorbecke, J., Verdel, A. and Wapenaar, K., 2009. Reflection images from ambient seismic noise: Geophysics, 74. A63-67.

Draganov D., Campman X., Thorbecke J. and Verdel A. 2013. Seismic exploration-scale velocities and structure from ambient seismic noise (>1 Hz). Journal of Geophysical Research: Solid Earth 118, 1–16.

Frster, A., Norden, B., Zinck-Jrgensen, K., Frykman, P., Kulenkampff, J., Spangenberg, E., Erzinger, J., Zimmer, M., Kopp, J., Borm, G. and Juhlin, C., 2006. Baseline characterization of the CO2SINK geological storage site at Ketzin, Germany. Environmental Geosciences, 13(3), pp.145-161.

Gerstoft, P., Sabra, K., Roux, P., Kuperman, W.A. & Fehler, M., 2006. Green's functions extraction and surface-wave tomography from microseisms in southern California, Geophysics, 71, SI23–SI32.

Gudmundsson,O.,Khan, A.&Voss, P., 2007. Rayleigh-wave group-velocity of the Icelandic crust from correlation of ambient seismic noise, Geophys.Res. Lett. 34, L14314, doi: 10.1029/2007GL030215.

Halliday, D. & Curtis, A., 2008. Seismic interferometry, surface waves and source distribution, Geophys. J. Int., 175, 1067–1087.

Halliday, D., Curtis, A. & Kragh, E., 2008. Seismic surface waves in a suburban environment: active and passive interferometric methods, Leading Edge, 27, 210–218.

Hurich C. and Deemer S. 2013. Combined surface and borehole seismic imaging in a hard rock terrain: a field test of seismic interferometry. Geophysics 78, B103−B100.

Korneev, V., Bakulin, A. and Lopez, J., 2008. Imaging and monitoring with virtual sources on a synthetic 3D data set from the Middle East.

Kumar, M.R. and Bostock, M.G., 2006. Transmission to reflection transformation of teleseismic wavefields. Journal of Geophysical Research: Solid Earth, 111(B8).

Larose E., Derode, A., Campillo, M. & Fink, M., 2004. Imaging from one-bit correlations of wide-band diffuse wavefield, J. appl. Phys., 95, 8393–8399.

Larose, E. et al., 2006b. Correlation of random fields: an interdisciplinary review, Geophysics, 71, SI11–SI21.

Larose, E., Lobkis, O.I. &Weaver, R.L., 2006a. Passive correlation imaging of a buried scatterer, J. acoust. Soc. Am., 119, 3549–3552.

Lumley, D.E., 2001. Time-lapse seismic reservoir monitoring. Geophysics, 66(1), pp.50-53.

Mehta, K., Snieder, R. and Graizer, V., 2007. Extraction of near-surface properties for a lossy layered medium using the propagator matrix.Geophysical Journal International, 169(1), pp.271-280.

Mehta, K., Snieder, R., Calvert, R. and Sheiman, J., 2008. Acquisition geometry requirements for generating virtual-source data. The Leading Edge, 27(5), pp.620-629.

Nakata, N. and Snieder, R., 2012. Estimating near-surface shear wave velocities in Japan by applying seismic interferometry to KiK-net data.Journal of Geophysical Research: Solid Earth, 117(B1).

Nazarian, S., Stokoe, K.H. & Hudson, W.R., 1983. Use of spectral analysis of surface waves method for determination of moduli and thicknesses of pavement systems, Transport. Res. Record, 930, 38–45.

Nicolson, H., Curtis, A., Baptie, B. and Galetti, E., 2012. Seismic interferometry and ambient noise tomography in the British Isles.Proceedings of the Geologists' Association, 123(1), pp.74-86.

Panea, I., Draganov, D., Almagro Vidal, C. and Mocanu, V., 2014. Retrieval of reflections from ambient noise recorded in the Mizil area, Romania.Geophysics, 79(3), pp.Q31-Q42.

Prieto, G. A., J. F. Lawrence, and G. C. Beroza (2009), Anelastic Earth structure from the coherency of the ambient seismic field, J. Geophys. Res., 114, B07303, doi: 10.1029/2008JB006067.

Quiros, D.A., Brown, L.D. and Kim, D., 2016. Seismic interferometry of railroad induced ground motions: body and surface wave imaging. Geophysical Journal International, 205(1), pp.301-313.

Ritzwoller, M., Shapiro, N., Pasyanos, M., Bensen, G. & Tang, Y., 2005. Short-period surface wave dispersion measurements from ambient seismic noise in North Africa, the Middle East, and Central Asia, in Proceedings of 27th Seismic Research Review : Ground-Based Nuclear Explosion Monitoring Technologies, Palm Springs, CA, pp. 161–170.

Roux, P., Sabra, K.G., Gerstoft, P., Kuperman, W.A. and Fehler, M.C., 2005. P-waves from cross-correlation of seismic noise. Geophysical Research Letters, 32(19).

Sabra, K. G., P. Gerstoft, P. Roux, and W. A. Kuperman (2005), Surface wave tomography from microseisms in Southern California, Geophys. Res. Lett., 32, L14311, doi: 10.1029/2005GL023155.

Schuster, G. T., J.Yu, J. Sheng, and J. Rickett, 2004, Interferometric/daylight seismic imaging: Geophysical Journal International, 157, 838–852.

Schuster, G.T. and Zhou, M., 2006. A theoretical overview of model-based and correlation-based redatuming methods. Geophysics, 71(4), pp.SI103-SI110.

Schuster, G.T., 2001, June. Theory of Daylight/Interferometric Imaging-Tutorial. In 63rd EAGE Conference & Exhibition.

Sens-Schönfelder, C. and Wegler, U., 2006. Passive image interferometry and seasonal variations of seismic velocities at Merapi Volcano, Indonesia.Geophysical research letters, 33(21).

Shapiro, N.M., Campillo, M., Stehly, L. & Ritzwoller, M.H., 2005. High resolution surface-wave tomography from ambient seismic noise, Science, 307(5715), 1615–1618.

Shapiro, N. & Campillo, M., 2004. Emergence of broadband Rayleighwaves from correlations of the ambient seismic noise, Geophys. Res. Lett., 31, L07614, doi: 10.1029/2004GL019491.

Snieder, R., 2004. Extracting the Green's function from the correlation of coda waves: A derivation based on stationary phase. Physical Review E, 69(4), p.046610.

Snieder, R., Sheiman, J. and Calvert, R., 2006. Equivalence of the virtual-source method and wave-field deconvolution in seismic interferometry.Physical Review E, 73(6), p.066620.

Tonegawa, Takashi, Kiwamu Nishida, Toshiki Watanabe, and Katsuhiko Shiomi. "Seismic interferometry of teleseicmic S-wave coda for retrieval of body waves: an

application to the Philippine Sea slab underneath the Japanese Islands." Geophysical Journal International 178, no. 3 (2009): 1574-1586.

Vasconcelos I., Snieder R. and Hornby B. 2008. Imaging internal multiples from subsalt VSP data—examples of target-oriented interferometry. Geophysics 73, S157–S168.

Vasconcelos, I. and Snieder, R., 2008. Interferometry by deconvolution: Part 1—Theory for acoustic waves and numerical examples. Geophysics, 73(3), pp.S115-S128.

Wapenaar, K., Slob, E. and Snieder, R. (2008), Seismic and electromagnetic controlled-source interferometry in dissipative media. Geophysical Prospecting, 56: 419–434. doi: 10.1111/j.1365-2478.2007.00686.x

Wapenaar, K., Thorbecke, J. and Draganov, D., 2004. Relations between reflection and transmission responses of three-dimensional inhomogeneous media. Geophysical Journal International, 156(2), pp.179-194.

Weaver and Lobkis (2002) Ultrasonics Volume 40, Issues 1–8, May 2002, Pages 435–439 On the emergence of the Green's function in the correlations of a diffuse field: pulse-echo using thermal phonons.

Weaver, R. L., and O. I. Lobkis, 2001, Ultrasonics without a source:Thermal fluctuation correlations at MHz frequencies: Physical Review Letters, 87, 134301-1–134301-4.

Xu, Z., Juhlin, C., Gudmundsson, O., Zhang, F., Yang, C., Kashubin, A. and Lüth, S., 2012. Reconstruction of subsurface structure from ambient seismic noise: an example from Ketzin, Germany. Geophysical Journal International, 189(2), pp.1085-1102.

Yao, H., van der Hilst, R.D. & de Hoop, M.V., 2006. Surface-wave array tomography in SE Tibet from ambient seismic noise and two-station analysis: I—phase velocity maps, Geophys. J. Int., 166, 732–744.

Zhang, J., Gerstoft, P. and Shearer, P.M., 2009. High-frequency P-wave seismic noise driven by ocean winds. Geophysical Research Letters, 36(9).

9. Appendix A: Velocity analysis at CMP5600

(a) Before velocity picking

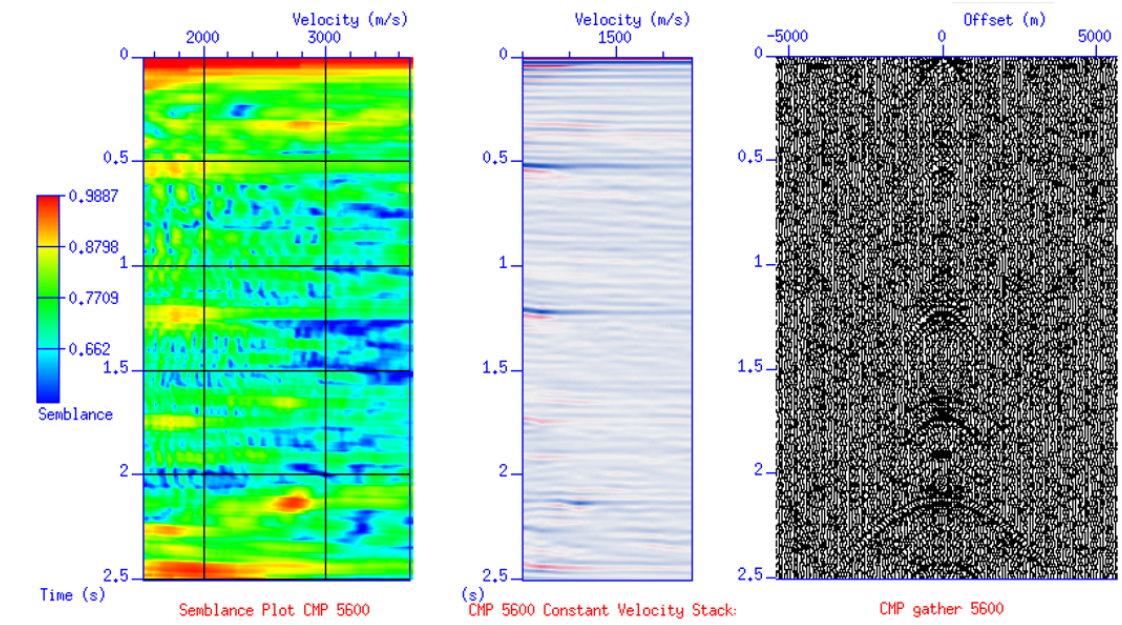

(b) After velocity picking

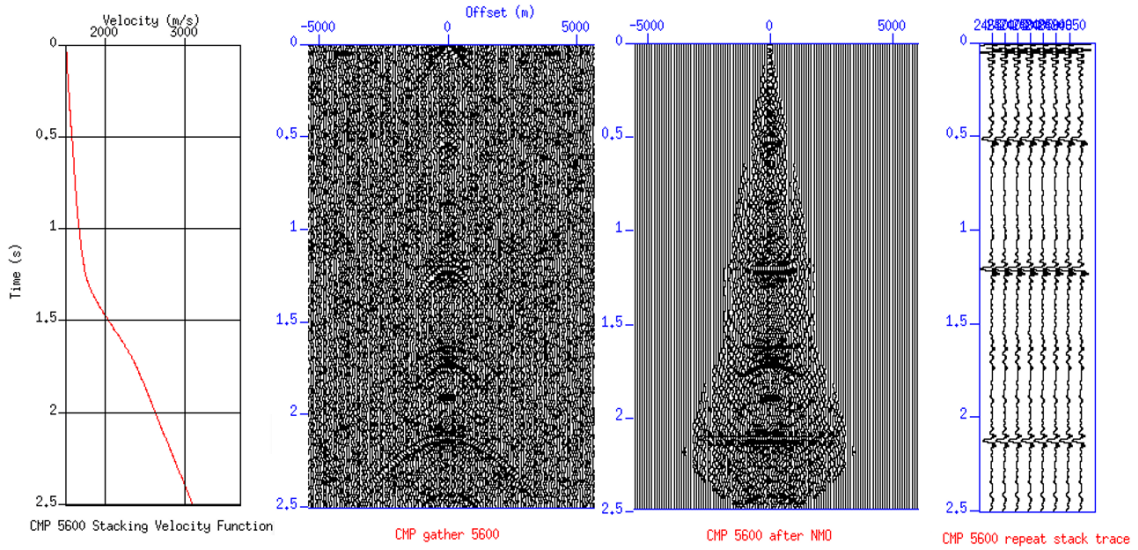

Figure 9.1. An example display for Velocity analysis for CMP5600. (a) shows the velocity spectrum contour plot, the semblance plot and CMP gather before picking. (b) shows the red line indicating the curve for NMO velocity, CMP gather before NMO correction, CMP gather after NMO correction and a stacked gather.

10. Appendix B: The velocity analysis for anticline case before CO_2 injection

cdp=2000,2200,2400,2600,2800,3000,3200,3400,3600,3800,4000,4200,4400,4600,480
0,5000,5200,5400,5600,5800,6000,6200,6400,6600,6800,7000,7200,7400,7600,7800 \

#=1,2,3,4,5,6,7,8,9,10,11,12,13,14,15,16,17,18,19,20,21,22,23,24,25,26,27,28,29,30 \

tnmo=0.0132137,0.535156,1.22227,1.7376,2.1142,2.51061 \

vnmo=1528.67,1614.67,1786.67,2560.67,2747,3220 \

tnmo=0.0264274,0.541763,1.21566,1.7376,2.1208,2.51061 \

vnmo=1528.67,1700.67,1844,2589.33,2747,3205.67 \

tnmo=0.0132137,0.528549,1.20906,1.75082,2.09437,2.51721 \

vnmo=1528.67,1657.67,1786.67,2575,2732.67,3191.33 \

tnmo=0.0132137,0.528549,1.22888,1.75082,2.1142,2.49739 \

vnmo=1528.67,1729.33,1872.67,2560.67,2747,3091 \

tnmo=0.0132137,0.528549,1.22888,1.74421,2.10098,2.49739 \

vnmo=1514.33,1643.33,1829.67,2489,2747,3162.67 \

tnmo=0.0132137,0.528549,1.22227,1.7376,2.10098,2.49739 \

vnmo=1528.67,1672,1815.33,2603.67,2675.33,3220 \

tnmo=0.0198206,0.521942,1.24209,1.78385,2.1142,2.51721 \

vnmo=1543,1614.67,1801,2646.67,2818.67,3062.33 \

tnmo=0.00660686,0.515335,1.22227,1.76403,2.10098,2.49739 \

vnmo=1528.67,1614.67,1729.33,2661,2747,3091 \

tnmo=0.0198206,0.548369,1.22888,1.75742,2.1142,2.49739 \

vnmo=1528.67,1600.33,1772.33,2618,2718.33,3134 \

tnmo=0.0132137,0.541763,1.22227,1.71118,2.1142,2.49739 \

vnmo=1528.67,1586,1801,2575,2761.33,3033.67 \

tnmo=0.0132137,0.521942,1.20245,1.69136,2.12741,2.51721 \

vnmo=1528.67,1629,1815.33,2532,2747,3134 \

tnmo=0.0198206,0.521942,1.22888,1.67154,2.1208,2.51061 \

vnmo=1528.67,1614.67,1786.67,2517.67,2675.33,3148.33 \

tnmo=0.0198206,0.521942,1.22227,1.65172,2.15384,2.504 \
vnmo=1528.67,1586,1786.67,2503.33,2732.67,3091 \
tnmo=0.0132137,0.521942,1.20906,1.63189,2.15384,2.504 \
vnmo=1528.67,1629,1743.67,2517.67,2732.67,3033.67 \
tnmo=0.0132137,0.528549,1.22227,1.63189,2.15384,2.51721 \
vnmo=1528.67,1600.33,1772.33,2417.33,2761.33,3119.67 \
tnmo=0.0198206,0.528549,1.20906,1.6385,2.15384,2.504 \
vnmo=1528.67,1614.67,1772.33,2489,2747,3105.33 \
tnmo=0.0132137,0.528549,1.20906,1.63189,2.14723,2.51061 \
vnmo=1528.67,1643.33,1772.33,2446,2646.67,2990.67 \
tnmo=0.0132137,0.541763,1.20245,1.62529,2.15384,2.51061 \
vnmo=1528.67,1657.67,1801,2446,2675.33,3062.33 \
tnmo=0.0264274,0.521942,1.23548,1.65832,2.13402,2.51061 \
vnmo=1528.67,1586,1743.67,2546.33,2761.33,3191.33 \
tnmo=0.0132137,0.528549,1.20906,1.67814,2.14062,2.504 \
vnmo=1528.67,1600.33,1786.67,2532,2689.67,3162.67 \
tnmo=0.0132137,0.521942,1.22227,1.69796,2.1208,2.51061 \
vnmo=1528.67,1629,1829.67,2589.33,2761.33,3148.33 \
tnmo=0.00660686,0.528549,1.20906,1.731,2.1208,2.53043 \
vnmo=1586,1729.33,1786.67,2618,2804.33,3306 \
tnmo=0.0198206,0.521942,1.20906,1.75742,2.1142,2.49739 \
vnmo=1614.67,1743.67,1858.33,2661,2804.33,3334.67 \
tnmo=0.0198206,0.495515,1.18263,1.77725,2.10759,2.51061 \
vnmo=1543,1643.33,1815.33,2575,2790,3234.33 \
tnmo=0.0198206,0.521942,1.22227,1.79707,2.10098,2.49079 \
vnmo=1543,1614.67,1815.33,2661,2790,3162.67 \
tnmo=0.0132137,0.515335,1.22227,1.77725,2.1208,2.51061 \
vnmo=1557.33,1643.33,1829.67,2618,2818.67,3148.33 \
tnmo=0.0198206,0.521942,1.21566,1.76403,2.10098,2.49739 \

vnmo=1571.67,1686.33,1815.33,2532,2775.67,3091 \

tnmo=0.0132137,0.541763,1.21566,1.76403,2.10759,2.504 \

vnmo =1557.33,1672,1801,2517.67,2790,3134 \

tnmo =0.00660686,0.548369,1.18923,1.77064,2.10098,2.504 \

vnmo =1543,1600.33,1686.33,2532,2775.67,3162.67 \

tnmo =0.0132137,0.541763,1.22227,1.76403,2.10759,2.51061 \

vnmo =1557.33,1614.67,1815.33,2532,2747,3091 \

11. Appendix C: The velocity analysis for anticline case after CO_2 injection

cdp=2000,2200,2400,2600,2800,3000,3200,3400,3600,3800,4000,4200,4400,4600,480
0,5000,5200,5400,5600,5800,6000,6200,6400,6600,6800,7000,7200,7400,7600,7800 \

#=1,2,3,4,5,6,7,8,9,10,11,12,13,14,15,16,17,18,19,20,21,22,23,24,25,26,27,28,29,30 \

tnmo=0.00660686,0.535156,1.20906,1.77064,1.82349,2.10759,2.49739 \

vnmo=1514.33,1571.67,1743.67,2603.67,2632.33,2704,3162.67 \

tnmo=0.0264274,0.528549,1.20906,1.75742,1.9292,2.1142,2.504 \

vnmo=1528.67,1586,1772.33,2603.67,2675.33,2775.67,3062.33 \

tnmo=0.0132137,0.535156,1.21566,1.77064,2.10759,2.51061 \

vnmo=1500,1571.67,1801,2618,2775.67,3162.67 \

tnmo=0.0198206,0.528549,1.21566,1.78385,2.1208,2.504 \

vnmo=1528.67,1600.33,1801,2589.33,2790,3148.33 \

tnmo=0.0132137,0.535156,1.20245,1.77064,2.10759,2.504 \

vnmo=1528.67,1600.33,1758,2560.67,2790,3048 \

tnmo=0.0264274,0.521942,1.22227,1.77725,2.10098,2.51061 \

vnmo=1528.67,1657.67,1801,2603.67,2804.33,3162.67 \

tnmo=0.0132137,0.528549,1.22227,1.77725,2.1142,2.49739 \

vnmo=1528.67,1600.33,1786.67,2661,2847.33,3105.33 \

tnmo=0.0198206,0.528549,1.22227,1.77064,2.1142,2.49079 \

vnmo=1528.67,1586,1772.33,2675.33,2790,3119.67 \

tnmo=0.0198206,0.541763,1.22227,1.76403,2.10759,2.49739 \
vnmo=1528.67,1629,1858.33,2618,2775.67,3205.67 \
tnmo=0.0132137,0.548369,1.22227,1.71778,2.10098,2.49079 \
vnmo=1528.67,1586,1815.33,2632.33,2790,3148.33 \
tnmo=0.0132137,0.521942,1.22888,1.69136,2.18687,2.49739 \
vnmo=1528.67,1571.67,1786.67,2603.67,2761.33,3162.67 \
tnmo=0.0132137,0.528549,1.22888,1.68475,2.1208,2.49079 \
vnmo=1514.33,1586,1758,2503.33,2589.33,2775.67 \
tnmo=0.0132137,0.528549,1.22227,1.64511,2.16044,2.49739 \
vnmo=1514.33,1586,1743.67,2503.33,2632.33,3019.33 \
tnmo=0.0198206,0.535156,1.22227,1.6385,2.15384,2.49739 \
vnmo=1528.67,1571.67,1772.33,2460.33,2661,2990.67 \
tnmo=0.0264274,0.535156,1.22888,1.62529,2.16705,2.504 \
vnmo=1543,1571.67,1743.67,2474.67,2646.67,2990.67 \
tnmo=0.0198206,0.541763,1.22227,1.63189,2.18687,2.504 \
vnmo=1543,1571.67,1743.67,2474.67,2689.67,3062.33 \
tnmo=0.0132137,0.541763,1.22888,1.62529,2.18026,2.51061 \
vnmo=1514.33,1614.67,1772.33,2417.33,2603.67,3105.33 \
tnmo=0.0198206,0.541763,1.21566,1.62529,2.16044,2.51061 \
vnmo=1543,1571.67,1758,2417.33,2575,2933.33 \
tnmo=0.0132137,0.528549,1.20245,1.65832,2.16705,2.51061 \
vnmo=1528.67,1557.33,1801,2517.67,2704,3048 \
tnmo=0.0198206,0.541763,1.22888,1.65832,2.17366,2.51061 \
vnmo=1543,1614.67,1829.67,2589.33,2546.33,2804.33 \
tnmo=0.0198206,0.521942,1.20245,1.69136,2.1142,2.51061 \
vnmo=1528.67,1586,1729.33,2546.33,2661,2876 \
tnmo=0.0198206,0.528549,1.19584,1.72439,2.22651,2.51061 \
vnmo=1543,1600.33,1729.33,2632.33,2847.33,3048 \
tnmo=0.0132137,0.548369,1.20245,1.75742,2.1142,2.51061 \

vnmo=1528.67,1629,1786.67,2646.67,2761.33,3005 \

tnmo=0.0264274,0.541763,1.20906,1.78385,2.1142,2.504 \

vnmo=1528.67,1586,1743.67,2646.67,2747,2990.67 \

tnmo=0.0132137,0.535156,1.22227,1.78385,2.1142,2.49739 \

vnmo=1528.67,1600.33,1729.33,2632.33,2775.67,2990.67 \

tnmo=0.0132137,0.528549,1.22888,1.7376,2.1142,2.51061 \

vnmo=1528.67,1614.67,1772.33,2603.67,2732.67,3076.67 \

tnmo=0.0132137,0.528549,1.22888,1.7376,2.1142,2.51061 \

vnmo=1543,1614.67,1786.67,2503.33,2732.67,2990.67 \

tnmo=0.0132137,0.528549,1.22227,1.77725,2.1208,2.51721 \

vnmo=1543,1600.33,1786.67,2603.67,2732.67,3076.67 \

tnmo=0.0198206,0.528549,1.22227,1.78385,2.09437,2.51061 \

vnmo=1528.67,1600.33,1801,2632.33,2761.33,2962 \

tnmo=0.0198206,0.554976,1.2487,1.76403,2.13402,2.504 \

vnmo=1528.67,1629,1815.33,2589.33,2747,3019.33 \